Cell Reports

Article

The zebrafish heart harbors a thermogenic beige fat depot analog of human epicardial adipose tissue

Graphical abstract

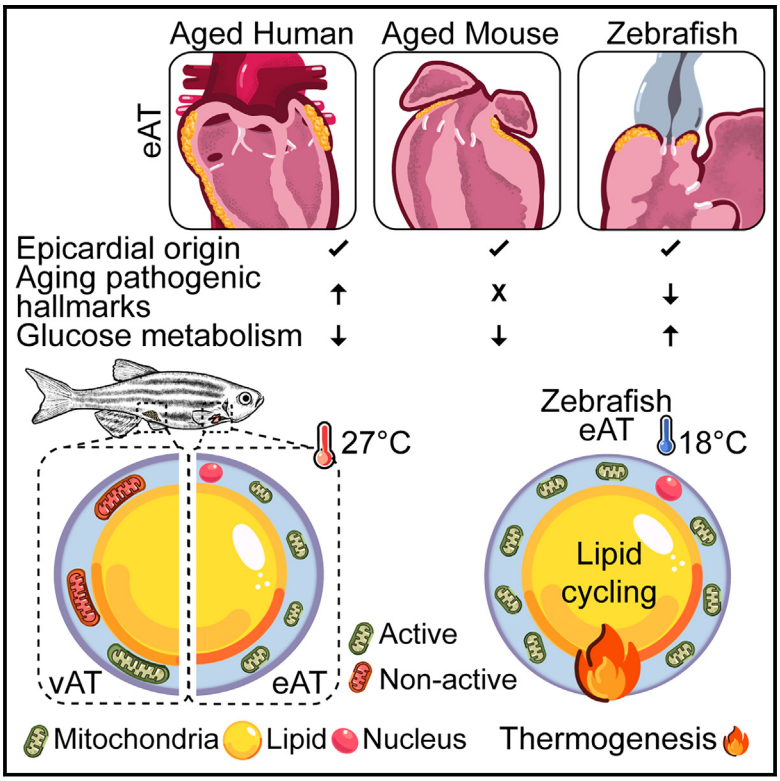

Authors

Paul-Andres Morocho-Jaramillo, Ilan Kotlar-Goldaper, Bhakti I. Zakarauskas-Seth, Bettina Purfürst, Alessandro Filosa, Suphansa Sawamiphak

Correspondence

suphansa.sawamiphak@mdc-berlin.de

In brief

Morocho-Jaramillo et al. identify metabolically active epicardial adipose tissue (eAT) in zebrafish, an ectotherm that has long been considered to possess only white adipose tissue. They show conserved and different transcriptomic features across vertebrate species and identify critical pathways that may underlie age-driven pathogenic transition in human eAT.

Highlights

- Zebrafish possesses cardiac fat analogous to human epicardial adipose tissue (eAT)
- A subpopulation of zebrafish eAT exhibits thermogenic capability
- Zebrafish eAT recapitulates beige transcriptome but suppresses human aging hallmarks
- Cold exposure augments lipid cycling and mitochondrial biogenesis in eAT

Morocho-Jaramillo et al., 2024, Cell Reports *43*, 113955
March 26, 2024
https://doi.org/10.1016/j.celrep.2024.113955

CellPress

Cell Reports

CellPress
OPEN ACCESS

Article

The zebrafish heart harbors a thermogenic beige fat depot analog of human epicardial adipose tissue

Paul-Andres Morocho-Jaramillo,[1,2] Ilan Kotlar-Goldaper,[1,2] Bhakti I. Zakarauskas-Seth,[1,2] Bettina Purfürst,[1] Alessandro Filosa,[1] and Suphansa Sawamiphak[1,3,*]

[1]Max-Delbrück-Center for Molecular Medicine in the Helmholtz Association (MDC), Robert-Rössle-Str. 10, 13125 Berlin, Germany
[2]Charité – Universitätsmedizin Berlin, Corporate Member of Freie Universität Berlin and Humboldt Universität zu Berlin, Berlin, Germany
[3]Lead contact
*Correspondence: suphansa.sawamiphak@mdc-berlin.de
https://doi.org/10.1016/j.celrep.2024.113955

SUMMARY

Epicardial adipose tissue (eAT) is a metabolically active fat depot that has been associated with a wide array of cardiac homeostatic functions and cardiometabolic diseases. A full understanding of its diverse physiological and pathological roles is hindered by the dearth of animal models. Here, we show, in the heart of an ectothermic teleost, the zebrafish, the existence of a fat depot localized underneath the epicardium, originating from the epicardium and exhibiting the molecular signature of beige adipocytes. Moreover, a subset of adipocytes within this cardiac fat tissue exhibits primitive thermogenic potential. Transcriptomic profiling and cross-species analysis revealed elevated glycolytic and cardiac homeostatic gene expression with downregulated obesity and inflammatory hallmarks in the teleost eAT compared to that of lean aged humans. Our findings unveil epicardium-derived beige fat in the heart of an ectotherm considered to possess solely white adipocytes for energy storage and identify pathways that may underlie age-driven remodeling of human eAT.

INTRODUCTION

The human heart is surrounded by a layer of fat, which accounts for about 20% of its total weight.[1] This adipose layer can cover 56%–100% of the heart surface.[2] Lying beneath the visceral pericardium is the epicardial adipose tissue (eAT).[3] The eAT is the only adipose tissue that is contiguous with the myocardium without a fascial barrier and is perfused by coronary arteries.[4] Besides this peculiar anatomical location, the eAT exhibits a beige-like molecular signature that differs from those of other fat depots.[4–7] Based on its unobstructed proximity to the myocardium, vascularization by coronary vessels, and expression of thermogenic and metabolic genes, numerous physiological roles for eAT in heart metabolism, insulation, and buffering from excess fatty acids have been proposed.[3,8,9] By contrast, under metabolic stress, the eAT, as a local source of ectopic lipids, can also be highly detrimental in the onset and progression of cardiovascular diseases, including coronary artery disease (CAD), atrial fibrillation, and heart failure, and might even serve as a reservoir and amplifier of severe acute respiratory syndrome coronavirus 2 (SARS-CoV-2).[9,10] Empirical evidence in support of these putative roles of the eAT is, however, still scarce. A major limitation of our understanding of eAT biology is the dearth of animal models with a well-characterized fat depot sharing anatomical, biochemical, and molecular properties with the human one.[11] Characterization of the human eAT has some limitations, since only postmortem samples or those obtained from patients who underwent cardiac surgery can be used for analyses.[12] Obtaining information about the tissue dynamics and physiological functions from these samples is complicated by aging and other comorbidities. A robust model system enabling *in vivo* manipulation to elucidate cellular and molecular mechanisms underlying the interactions between the epicardial adipocytes and cardiac and vascular cells is much needed.

In addition to the largely unknown physiological roles of the fat depot, there is its enigmatic evolution. Human eAT expresses the brown adipocyte-specific mitochondrial protein uncoupling protein 1 (UCP1), a primary catalyst of proton dissipation without adenosine triphosphate (ATP) generation, implying the capability to release heat under cold stimuli.[5–7,13] As thermogenic activity implicates improvement of lipoprotein homeostasis and energy expenditure,[14,15] the biological function of UCP1 in human eAT is of much interest. Intriguingly, UCP1 orthologs have been identified in ectothermic vertebrates, refuting the presumption that UCP1 and brown adipose tissue emerged in placental mammals ~150 million years ago to survive cold environments.[16] Interestingly, some ectothermic species, like the common carp (*Cyprinus carpio*) and zebrafish (*Danio rerio*) can induce expression of UCP gene orthologs in the brain following cold exposure.[17,18] Moreover, the presence of "brown-like" multilocular adipocytes with a cold-induced aerobic-to-glycolytic metabolic shift was recently described in the brain of the lamprey, an ancient vertebrate that appeared 520 million years ago.[19] Collectively, these studies posit the intriguing hypothesis that the eAT may have

evolved much earlier than the appearance of Placentalia and may enable heart-specific thermogenesis or protection against oxidative stress by lowering mitochondrial proton gradients.

Here, we identified a cardiac fat depot in zebrafish that recapitulates the tissue localization, cellular origin, subcellular architecture, and molecular hallmarks of the beige mammalian eAT. Moreover, we found that a subpopulation of zebrafish cardiac adipocytes exhibits thermogenic ability, which is augmented by cold challenge, providing evidence of the existence of beige-like adipocytes in a teleost. Transcriptomic analyses comparing zebrafish, mouse, and human eAT unveiled a similarity in the metabolically active molecular signatures between the teleost and human fat depots, which are not shared by the murid rodent. By contrast, expression levels of several mediators of immune priming and pathogenic remodeling observed in aged human eAT are lower in the teleost fat depot. Hence, our findings not only present a model system that recapitulates hallmarks of human eAT but also suggest that the teleost fat depot may closely resemble healthy human eAT. Owing to these features, zebrafish could provide an opportunity to shed some light onto the mechanistic underpinnings of the proposed beneficial and detrimental roles of the human eAT under physiological conditions and upon metabolic challenges.

RESULTS

The zebrafish heart harbors a highly innervated fat depot that is vascularized by coronary vessels

Studies of eAT physiology thus far have relied mainly on biopsies from patients who underwent cardiac surgery, since samples from healthy subjects are not available for ethical reasons. This strategy has clear limitations for interpretation of the data obtained. In addition to cardiovascular risk factors, old age of the subjects can profoundly influence both morphology and function of the eAT.[20] Although little is known about age-related eAT remodeling, pronounced genotypic and phenotypic adaptations observed in human and mammalian models have suggested decreased brown adiposity, characterized by a shift of expression from thermogenesis- to lipogenesis-related genes, and suppression of cardioprotective adipokine expression during the dynamic transition from the post-natal period to adulthood.[21–24] While adipose tissue covers the majority of the heart surface in adult humans,[1] the presence of eAT in the embryonic heart is more restricted, initially detectable during gestation in the cardiac bulbus and atrioventricular groove, and expands caudally along developing coronary vessels.[24] Remarkably, our histological examination of adult zebrafish hearts revealed fat tissue in these anatomical locations. Zebrafish cardiac adipocytes, visualized by the lipophilic dye BODIPY, were localized mainly at the bulbo-ventricular boundary (Figures 1A and 1B). Some of these fat cells were in contact with large coronary arteries (Figures 1B and 1C) and interspersed among smaller branches (Figures 1D, 1E, and S1A), fluorescently labeled in the transgenic line *kdrl:HRAS-mCherry*, suggesting perfusion of the fat depot by the coronary vascular system that also supplies the myocardium. In addition to being highly vascularized, visualization of the cardiac autonomic nerves with anti-acetylated tubulin immunofluorescence staining showed that the zebrafish cardiac fat depot was densely innervated (Figures 1F, 1G, and S1B).

The epicardium gives rise to the cardiac adipose tissue

Beside specific localization, association with coronary vessels, and autonomic innervation that resembles distinctive characteristics of the mammalian eAT, we further examined the relation of these fat cells with the epicardial layer. Anti-aldehyde dehydrogenase (Aldh1a2) immunostaining of epicardial cells showed that these adipocytes lay underneath the epicardium (Figures 1H and 1I). Mammalian eAT originates from the epicardium through mesenchymal transition.[11,25,26] This specific cellular origin is also conserved in the zebrafish cardiac adipocytes observed here. Using the transgenic line *cryaa:EGFP; tcf21:Cre-ERT2; -3.5ubb:loxP-EGFP-loxP-mCherry*, we lineage-traced epicardial cells, which expressed the Cre-ERT2 recombinase under the control of the proepicardial marker gene *tcf21* during the embryonic stage. By applying 4-hydroxytamoxifen (4-OHT) 1–2 days post fertilization (dpf), we induced excision of the EGFP-coding sequence from the *-3.5ubb:loxP-EGFP-loxP-mCherry* transgene, allowing permanent expression of mCherry by the ubiquitous ubiquitin B (*ubb*) promoter (Figure 1J). Flow cytometry analysis of *tcf21:CreERT2*-traced cells showed that epicardial cells contribute, on average, 72% of eAT adipocytes (Figures 1K–1M). Notably, this tracing strategy may not target all epicardial cells in the developing heart (Figures S1C–S1E) and may underestimate the epicardial contribution to cardiac adipocytes.

Zebrafish cardiac adipose tissue exhibits molecular characteristics and subcellular architecture of metabolically active beige adipocytes

The beige nature of the eAT (i.e., heterogeneous cell populations arising from browning of white adipocytes) is reflected in their expression of different white and brown adipocyte markers.[6,7] Interestingly, zebrafish cardiac adipocytes contained the brown/beige adipocyte-specific mitochondrial membrane protein Ucp1, which confers the adaptive non-shivering thermogenic capacity to brown/beige adipocytes, as well as Hoxc8 and Hoxc9, two markers of white adipocytes (Figures 2A and S2), suggesting conservation of the beige characteristics. The findings are rather unexpected given that previously characterized zebrafish fat depots have been shown to be homologous to mammalian white adipose tissue.[27] Of note, Prdm16, a transcription factor known to stimulate brown adipogenesis, was not detectable in zebrafish cardiac adipocytes (Figure 2A), suggesting that molecular differences exist between the teleost tissue and the mammalian brown/beige fat depot.

In addition to the molecular characterization of these epicardium-derived adipocytes in zebrafish, we also examined their subcellular structures. A key feature distinguishing white and brown/beige adipocytes is mitochondrial morphology. Dynamic morphological adaption of mitochondria from an elongated to a more fragmented shape occurs by sympathetically induced mitochondrial fission to increase mitochondrial uncoupling and energy expenditure.[28,29] Transmission electron microscopy indeed showed a rounder architecture of mitochondria in zebrafish epicardial adipocytes compared with those of typical white

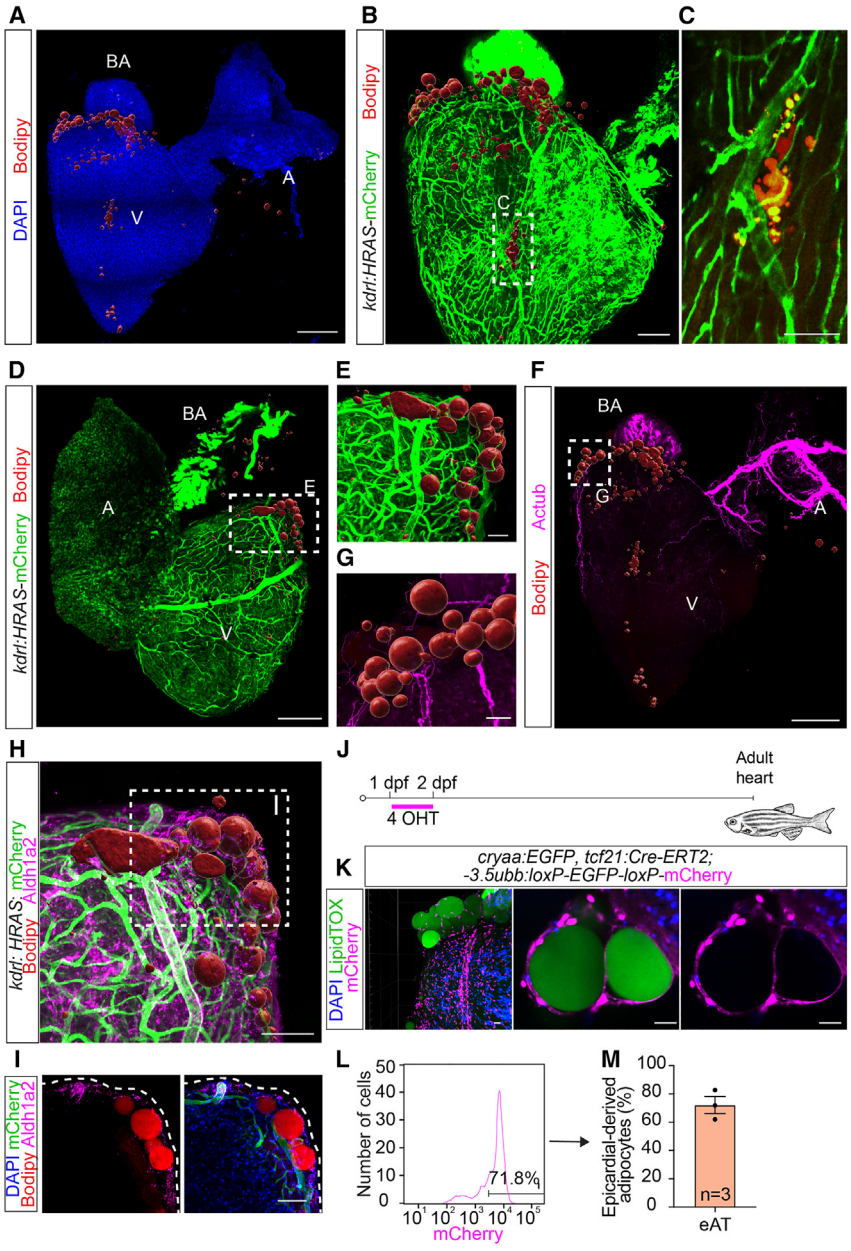

Figure 1. Anatomical localization, subtissular niche, and epicardial origin identify a zebrafish cardiac fat depot equivalent to the mammalian eAT

(A) Zebrafish eAT localizes mainly at the anterior pole of the heart. Shown is a confocal image of an adult zebrafish heart stained with BODIPY 558/568 C12 to detect lipids (adipocytes) and DAPI. Scale bar, 200 μm.

(B and C) Zebrafish eAT is in contact with major coronary vessels.

(B) A *kdrl:Has.HRAS-mCherry* zebrafish heart, immunostained for mCherry and stained with BODIPY 558/568 C12. Scale bar, 100 μm.

(C) Enlargement of the boxed area in (B). Scale bar, 50 μm.

(D and E) Vascularization of zebrafish eAT by underlying coronary vessels.

(D) A *kdrl:Has.HRAS-mCherry* zebrafish heart, immunostained for mCherry and stained with BODIPY 558/568 C12. Scale bar, 200 μm.

(E) Enlargement of the boxed area in (D). Scale bar, 50 μm.

(F and G) Zebrafish eAT is highly innervated.

(F) Heart immunostained for acetylated tubulin (Actub). Adipocytes were visualized with BODIPY 558/568 C12 staining. Scale bar, 200 μm.

(G) Digitally traced nerves from the boxed area in (F). Scale bar, 50 μm.

(H and I) The fat depot is located underneath the epicardium.

(H) Adult *kdrl:Has.HRAS-mCherry* zebrafish heart, immunostained for the epithelial marker Aldh1a2 and mCherry. Adipocytes were visualized with BODIPY 558/568 C12 staining. Scale bar, 50 μm.

(I) A single confocal plane of the boxed region in (H). Scale bar, 50 μm.

(J and K) Epicardial origin of zebrafish eAT.

(J) Schematic of the epicardial linage tracing approach. 4-OHT-mediated induction of Cre recombination in *tcf21:Cre-ERT2; ubb:loxP-EGFP-loxP-mCherry* fish at 1–2 days post fertilization (dpf) enabled labeling of cells derived from tcf21+ pro-epicardial cells in the adult heart.

(K) Epicardium-derived cells were visualized by mCherry immunostaining and adipocytes by LipidTOX. DAPI labeled all cell nuclei in the heart. Scale bar, 20 μm.

(L) Representative flow cytometry plot showing distribution of *tcf21:Cre-ERT2* traced cells by mCherry fluorescence intensities.

(M) Graph showing average percentage of mCherry+ epicardium-derived adipocytes in the zebrafish heart.

V, ventricle; A, atrium; BA, bulbus arteriosus. Adipocytes in (A), (B), and (D)–(H) are shown as 3D surface-rendered objects. All images represent observations from 3 animals per group.

adipocytes from the abdominal visceral adipose tissue (vAT) (Figures 2B–2D). Mitochondrial density per cytoplasmic area was similar in these two types of cells (Figure 2E).

Thermogenic capability of the ectothermic teleost eAT

Like most ectotherms, thermogenesis has not been reported in zebrafish fat depots. Interestingly, treatment of heart explants with forskolin, an adenylate cyclase activator, or carbonylcyanide-3-chlorophenylhydrazone (CCCP), a mitochondrial uncoupler, which mimic adrenergic receptor signaling-induced thermogenesis in adipocytes, induced heat production in zebrafish eAT, as measured by a ratiometric mito-thermometry method using the mitochondrion-specific thermoneutral and thermosensitive dyes MitoTracker Deep Red (MTDR) and tetra-methyl rhodamine methyl ester (TMRM)[30] (Figures 2F–2J). In accord with the metabolically active characteristic of this tissue, accumulation of both TMRM and MTDR that depends on mitochondrial membrane potential was higher in the eAT compared to vAT (Figure S3). To corroborate the image-based analyses and measure the degree of heterogeneity in the thermogenic ability

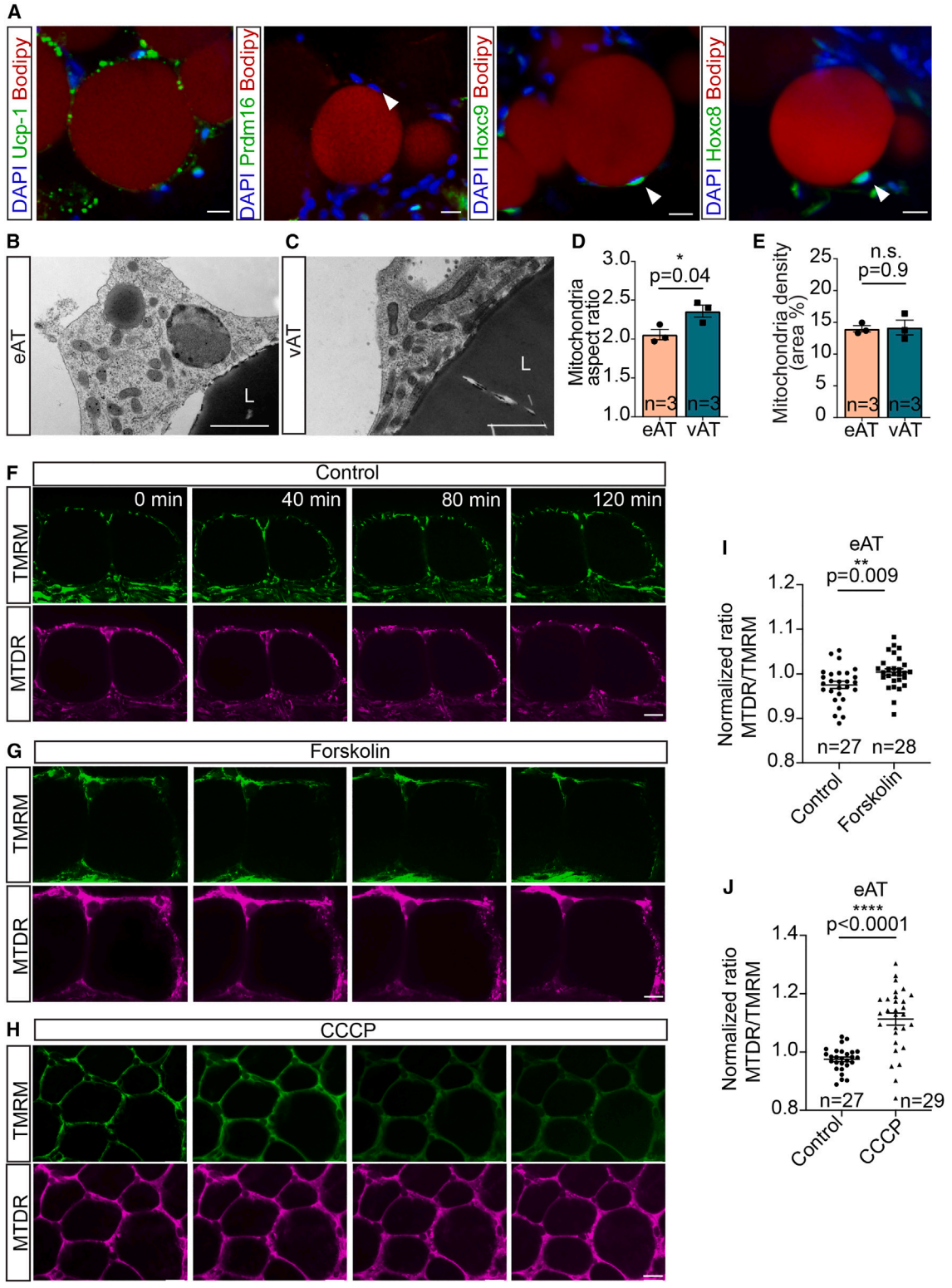

Figure 2. Zebrafish eAT possesses molecular signatures, subcellular morphology, and thermogenic capability typical of beige adipocytes

(A) Confocal images of zebrafish hearts immunostained for the brown/beige markers Ucp1 and Prdm16 or the white adipocyte markers Hoxc8 and Hoxc9 and stained with BODIPY 558/568 C12 and DAPI. Arrowheads indicate adipocyte nuclei. Scale bar, 10 μm.

(legend continued on next page)

of zebrafish eAT, we carried out flow cytometry analysis of adipocytes stained with the thermosensitive fluorescent dye ERthermAC.[31–33] ERthermAC accumulates in the endoplasmic reticulum (ER), and its fluorescence intensity is inversely correlated to temperature (i.e., the higher the temperature, the lower the fluorescence intensity), allowing direct monitoring of temperature fluctuations in live cells. In line with our observations in tissue explants, forskolin induced a clear shift of an epicardial adipocyte population to a higher temperature range (ERthermAC^{high} to ERthermAC^{low}). Compared with control vehicle treatment, where over 80% of adipocytes are ERthermAC^{high}, around 60% of the highly fluorescent cell population remained in the epicardial fat depot after forskolin stimulation (Figures 3A, 3B, and S4A). The forskolin-stimulated ERthermAC^{low} adipocyte subset was not present in adipocytes from the vAT (Figures 3C, 3D, and S4B). A reduction of lipid content, detectable by a neutral lipid stain, LipidTOX, was also evident in the ERthermAC^{low} compared with ERthermAC^{high} adipocytes from the heart but not from the abdomen (Figures 3E–3G), implying that forskolin-driven lipolysis fuels thermogenesis. Collectively, here we uncovered a cardiac fat depot in the teleost heart that not only shares specialized histological localization, subcellular architecture, and cellular origin with the mammalian eAT but also contains an adipocyte subset displaying thermogenic capacity typical of mammalian beige eAT.

Zebrafish eAT displays depot-specific expression of genes critical for energy expenditure and cardiac functional support

The presence of eAT or any beige adipose tissue in the heart of an ectotherm has not been reported earlier. To further validate the beige adipocyte molecular profile and cast some light on the physiological function of this previously unknown fat depot, we compared the transcriptomes of zebrafish eAT and vAT using RNA sequencing (RNA-seq) (Figure 4A). Only female samples were examined to prevent possible impact of sexual dimorphism on the eAT transcriptome. Transcriptomic analyses revealed that the eAT markedly upregulated different transcription factors with fundamental roles in cardiac development, including *gata4*, *tbx20*, and *tcf21*, a feature that has been shown to distinguish eAT from other fat depots in humans.[13] Moreover, relative to vAT, eAT highly expressed several genes with primary functions in mitochondrial respiration, beiging of white adipocytes, and noncanonical thermogenesis, such as *tfr1a*, *serca2*, and *ryr2b* as well as *cited1*, an established marker of beige adipocytes.[34,35] Upregulation of regulators of cardiac muscle contraction such as *tnnt2a*, *myh6*, *myh7l*, and *actc1a*, which is a key feature of human eAT,[7] was also detected in zebrafish cells (Figure 4B). By contrast, the homeobox (hox) gene family (*hoxc3a*, *hoxc8a*, and *hoxc9a*) along with pck1, which are classical white adipocyte markers, were downregulated in zebrafish eAT (Figure 4B). Flow cytometry analysis further revealed the presence of different subsets of eAT cells. Compared with vAT, a classical white adipose tissue of the abdomen in which high expression of Hoxc8 was detected in over 70% of all cells, eAT contained approximately 30% of Hoxc8^{high} adipocytes (Figures S5A–S5C). Expression of pivotal regulators of cardiac development and contractile function, cTnt and Tbx20, was also detected in approximately 5% of eAT cells (Figures S5A–S5C). Negligible proportions of cells expressing these genes were found in vAT (Figure S5D), and cTnt expression in some of the cardiac adipocytes was also confirmed by immunofluorescent staining (Figure S5E). In accord with the marked difference in the expression profiles, principal-component analysis (PCA) showed that, although there was higher individual variability among the vATs, the type of fat depot accounted for the largest variance of all samples (Figure 4C). The most overrepresented KEGG (Kyoto Encyclopedia of Genes and Genomes) pathways, determined from all differentially expressed genes (DEGs) between eAT and vAT, further revealed engagement of zebrafish eAT cells in adrenergic signaling, energy expenditure and glucose metabolism, cardiac muscle contraction, and calcium signaling (Figure 4D). These molecular pathways not only highlight specialized functional characteristics of the fat depot, which are conserved in humans,[7,36] but also suggest its strong interaction with the myocardium and the cardiac sympathetic nervous system.

Zebrafish eAT recapitulates the human eAT transcriptomic program, but pathogenic hallmarks of aging are less represented

The transcriptomic profile of zebrafish eAT implicated cardiac homeostatic functions, as postulated for the fat depot of "healthy" humans.[3,8,9] Transcriptomic characterization of young subjects without any type of cardiovascular disease, however, is not possible to achieve for ethical reasons. Expression profiling of human eAT upon cardiovascular diseases and comorbidities, particularly aging, metabolic syndrome, and diabetes, has highlighted involvement of the fat depot in several disease pathological processes, including inflammation, fibrosis, and thrombosis.[7,37] Interestingly, these pathogenic pathways were not overrepresented, and genes participating in the pathways were not differentially expressed in zebrafish eAT. To further characterize the similarity of zebrafish and human eAT and better understand the divergence of their molecular makeup, we carried out cross-species analysis

(B–E) Electron microscopy images depicting round and fragmented mitochondria in zebrafish eAT (B) compared with the elongated and tubular morphology common in adipocytes from visceral adipose tissue (vAT) (C). L, lipid droplet. Scale bar, 1 μm. A bar graphs show the mitochondrial aspect ratio in eAT and vAT (D) and mitochondrial density (per cytoplasmic area of individual cells) in eAT and vAT (E).

(F–J) Forskolin induces thermogenesis in the eAT.

(F–H) Still images captured from time-lapse imaging of explanted hearts show changes of fluorescence intensity in epicardial adipocytes, co-stained with MitoTracker Deep Red (MTDR) and tetra-methyl rhodamine methyl ester (TMRM), following vehicle (F), forskolin (G), or carbonylcyanide-3-chlorophenylhydrazone (CCCP) (H) treatment. Scale bars, 20 μm.

(I and J) Scatterplots showing increased thermal ratios (MTDR/TMRM) of epicardial adipocytes, stimulated by forskolin (I) or CCCP (J), compared with vehicle treatment.

Data in (D), (E), (I), and (J) are presented as mean ± SEM. n.s., not significant. *$p < 0.05$, **$p < 0.01$, ***$p < 0.001$, two-tailed t test. n indicates number of animals (D and E) and number of adipocytes obtained from three fish per condition (I and J).

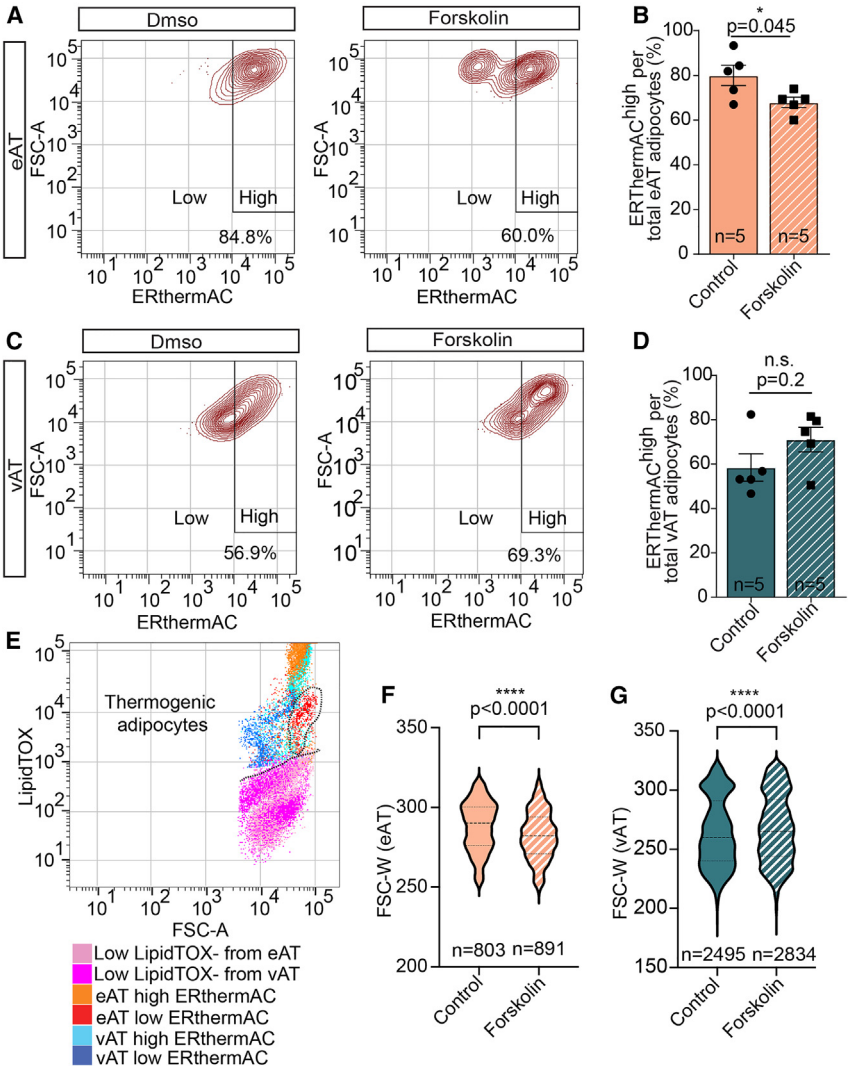

Figure 3. Heterogeneity of thermogenic activity, fueled by lipolysis in zebrafish eAT

(A) Representative contour plots of flow cytometry analysis revealing a forskolin-stimulated ERthermAC^{low} population in zebrafish eAT.

(B) Bar graph displaying a reduction of ERthermAC^{high} adipocytes in the eAT following forskolin exposure.

(C) Contour plots showing no detectable shift of intensity of ERthemAC by flow cytometry in the vAT adipocytes treated with forskolin compared with control solution-treated ones.

(D) Bar graph showing unaltered percentages of ERthemAC^{high} adipocytes in the vAT following forskolin exposure compared with controls.

(E) Dot plot showing lower lipid content (stained with LipidTOX) following forskolin stimulation in ERthemAC^{low} (thermogenic) compared with ERthemAC^{high} (non-thermogenic) adipocytes from eAT but not vAT. A dashed line encircles the thermogenic eAT population.

(F and G) Violin plots showing size distribution of epicardial (F) and abdominal (G) adipocytes before and after forskolin treatment. Middle lines indicate the median, and lower and upper lines indicate the first and third quartile, respectively.

Data in (B) and (D) are presented as mean ± SEM. *p < 0.05, ****p < 0.0001, two-tailed t test. n indicates number of animals (B and D) or number of cells from three fish per condition (F and G).

on the RNA-seq data from female zebrafish eAT and vAT and previously published human eAT and a classical white fat depot, subcutaneous adipose tissue (SAT), from the same individuals[13] (Figure 5A). We focused our analysis on lean females not diagnosed with CAD in the human study to minimize the influence of cardiometabolic conditions and sexual dimorphism. All patients were 75–80 years old. PCA showed that interspecies difference accounted for the largest variation among all samples. Zebrafish fat depots exhibited greater intraspecies variation than the human ones (Figure 5B). Based on the known one-to-one orthologs of DEGs from female zebrafish eAT relative to vAT and female human eAT relative to SAT, our analysis further validated conservation of the eAT-specific molecular signature. eAT from both species exhibits lower expression of the HOX family genes and elevation of key mediators of beige adipocyte differentiation and epicardial lineage markers; for example, TCF21, TRIM55, TBX20, and CPNE5 (Figures 5C, 5D, and S6).[38–40] Pathway analysis revealed overrepresentation of key regulators of mitochondrial respiration and metabolism that further support the thermogenic beige identity shared by both zebrafish and human eAT (Figure 5E). Enrichment of genes essential for the primary signaling pathway activated by ER stress, strongly associated with obesity and inflammation in white adipose tissue, was also a common feature of the classic white depots from both species (Figure 5F). On the other hand, our analysis unveiled intriguing differences between the eAT of the two species. Several genes were highly expressed in human eAT compared with SAT but downregulated in zebrafish eAT compared with vAT; for instance, BHLHA15, MAT1A, VIPR2, and VTN (Figure 5D), which play pivotal roles in pathogenesis of obesity, metabolic syndrome, and chronic inflammation mainly by driving inflammatory cell infiltration, cytokine synthesis, and ER stress.[41–45] Conversely, different zebrafish eAT-enriched genes that were downregulated in human eAT, such as IRX1, PGAM2, ALDOA, PFKP, and POSTN, are positive regulators of fat loss, glycolysis, and cardiac tissue homeostasis (Figure 5D).[46–50]

Mouse eAT does not exhibit age-related pathogenic remodeling characteristics of the human fat depot

Identification of the metabolically active eAT and its transcriptomic profile in an ectothermic teleost calls for better understanding of the evolutionary conservation of cardiac homeostatic function of the fat depot and its decline by age-related remodeling. Toward this end, we carried out RNA-seq of young (6 weeks old) and aged (24 months old) mouse fat tissue isolated from the atrioventricular groove. Of note, restricted coverage of eAT was similar in the hearts of young and old mice (Figure 6A). Unexpectedly, marked changes

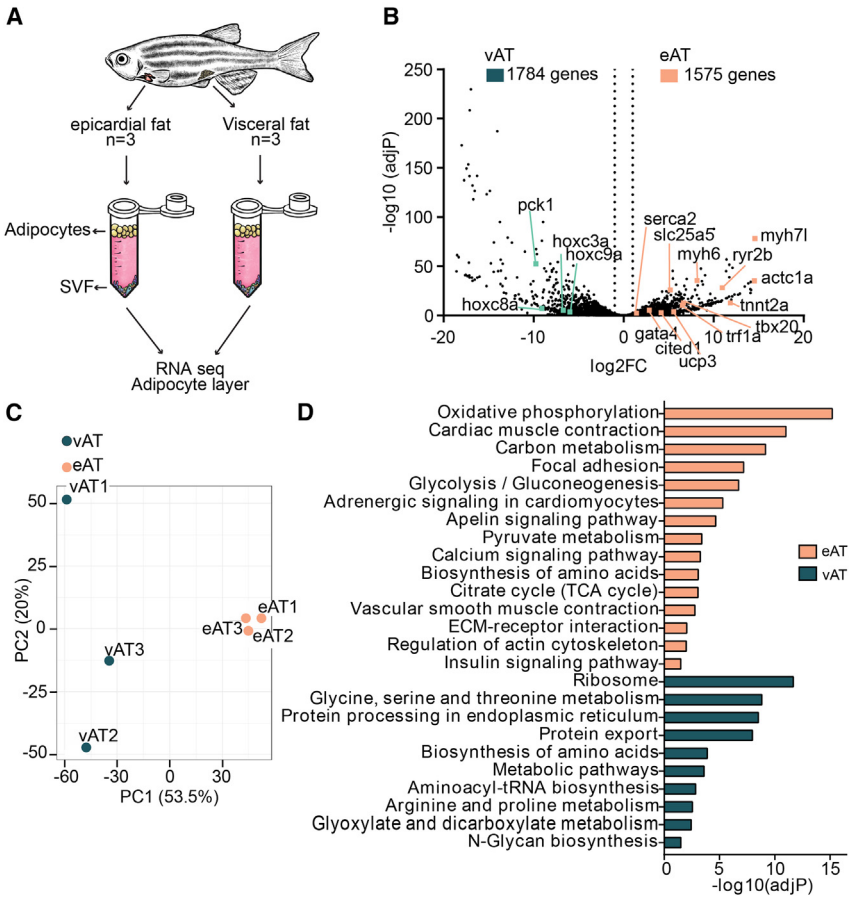

Figure 4. RNA-seq of adipocytes isolated from eAT and vAT reveals markedly different genome-wide expression profiles between the fat depots

(A) Schematic of the bulk RNA-seq approach for isolated adipocytes. SVF, stromal vascular fraction.
(B) Volcano plot displaying differentially expressed genes in eAT compared with vAT. The x axis shows fold change on a log2 scale and the y axis adjusted p value on a −log10 scale. A total of 1,575 genes were upregulated in zebrafish eAT and 1,784 genes in the vAT.
(C) Principal-component analysis (PCA) score plot showing clustering of adipocytes based on tissue type.
(D) KEGG enrichment pathways from differentially expressed genes in the eAT versus vAT, expressed as the −log10[P] adjusted for multiple comparisons. Data were obtained from 3 animals per group.

upon aging were upregulation of metabolic activity and downregulation of extracellular matrix-associated signaling, as evidenced from the top most differentially expressed genes (Figure 6B) and enriched pathways (KEGG and Reactome) (Figures S7A and S7B). Compared with human and zebrafish, PCA showed that both young and aged mouse eAT were both clustered closely to human eAT based on principal component 1 (PC1), for which taxonomic class was predicted to be the main contributor of the variance (Figures 6C and 6D). However, considering PC2, largely accounting for different tissue profiles, young and aged mouse eAT clusters were very similar, suggesting that, relative to the difference among fat tissues of all species analyzed, aging does not remarkably alter the expression profile of the mouse eAT (Figures 6C and 6D). Interestingly, according to PC2, the transcriptomic difference between zebrafish and human fat depots was smaller than between mouse and human (Figures 6C and 6D). Furthermore, cross-species comparative analysis of DEGs revealed that human and zebrafish eAT, but not mouse eAT, are characterized by a transcriptional program typical of metabolically active brown/beige adipose tissue, including adrenergic signaling, lipolysis, and fatty acid and glucose metabolism (Figures 6E, 6F, and S7C). By comparison, overrepresented genes involved in intercellular signaling, which was a common feature between the mammalian eAT, were not shared by the teleost fat depot (Figures 6E, 6F, and S7D). In summary, our results reveal that, unlike human eAT, mouse eAT may not serve critical metabolic functions or undergo significant remodeling upon aging.

Cold exposure induces a transcriptomic response in zebrafish eAT to augment lipid cycling and mitochondrial biogenesis

To better define the role of eAT in the maintenance of cardiac homeostasis, we subjected zebrafish to cold challenge. Female zebrafish were acclimatized to a cold environment (9°C lower than ambient temperature, from 27°C to 18°C) for 24 h (Figure 7A). Interestingly, RNA-seq of isolated eAT showed that the cold challenge, while inducing a clear transcriptomic adaptation (Figure 7B), did not alter levels of different mitochondrial uncoupling genes expressed in the fat depot, including *ucp1*, *ucp2*, and *ucp3* (Figures 7C and 7D). By comparison, cold exposure stimulated eAT expression of critical regulators of lipolysis, fatty acid mobilization into the mitochondria, fatty acid oxidation, and triacylglyceride re-synthesis; for example *cpt1b*, *cpt1ab*, *acsl1b*, *pnpla2*, *plpp2*, *agpat3*, *gpd1b*, and *acot15* (Figure 7C). Additionally, cold-exposed eAT markedly upregulated several genes with key roles in glycolysis and mitochondrial biogenesis and turnover, such as *tpi1a*, *gpd1b*, *prkn*, *atg9a*, *tbk1*, u*lk1a*, *tfeb*, and *tax1bp1b* (Figure 7E). The transcriptomic profiles thus suggest that cold challenge induces a transcriptomic response in zebrafish eAT to drive an Ucp1-independent and lipid cycling-dependent thermogenic machinery.[51] In support of the transcriptomic data, MitoTracker staining showed an increase in active mitochondria following cold exposure (Figure 7F). Together, these findings suggest that eAT plays a role in thermoregulation of the heart in cold challenge.

DISCUSSION

The presence of eAT has not been reported in non-mammalian vertebrates. Zebrafish, as most ectotherms, are commonly viewed to have only white adipocytes.[52] Here we uncovered a zebrafish

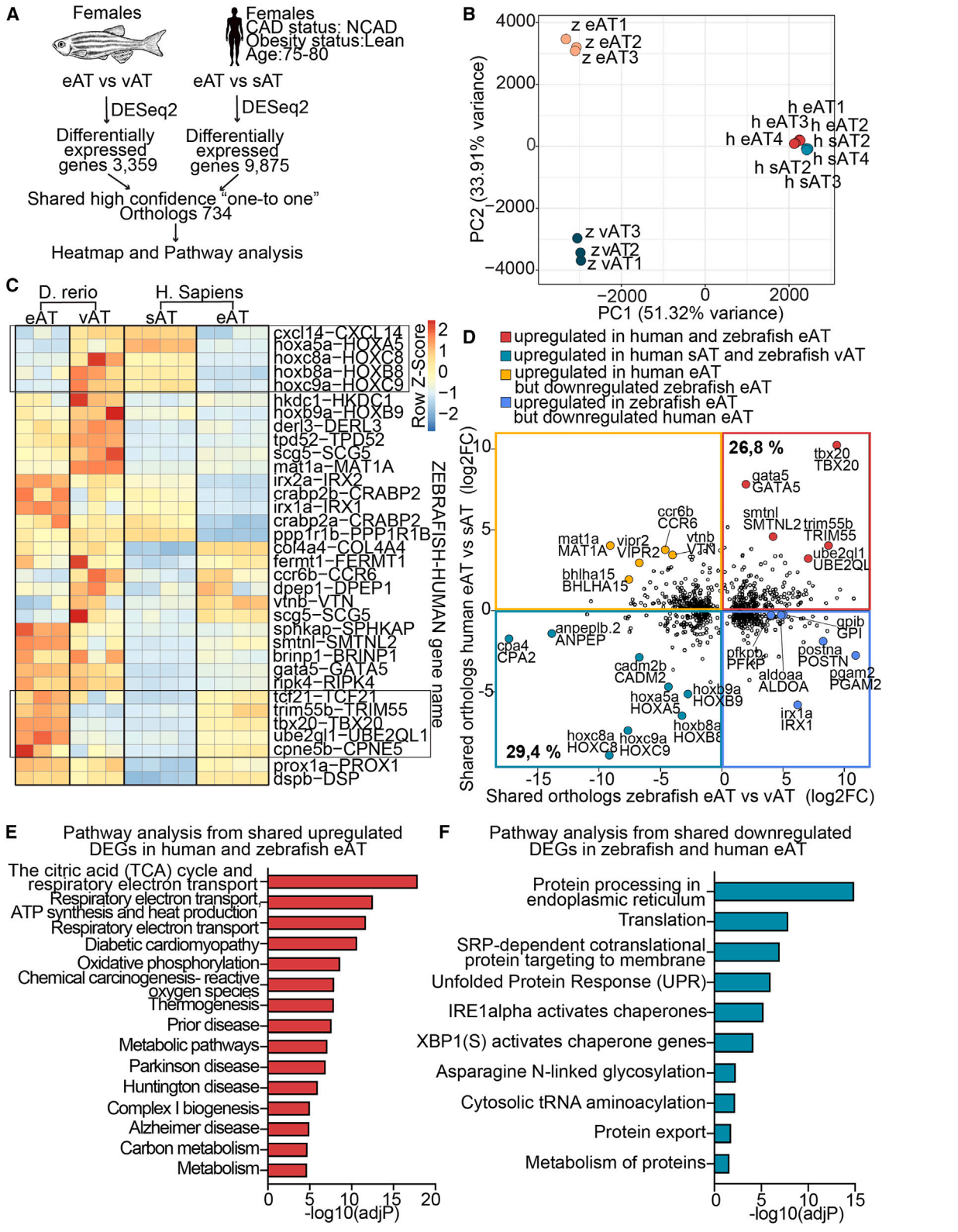

Figure 5. Comparative analysis of the transcriptomic profiles of zebrafish and healthy human epicardial adipocytes

(A) Schematic of the cross-species analysis focusing on high confidence "one-to-one" orthologs between zebrafish and human genes.

(B) PCA score plot showing clustering of adipocyte populations according to species and tissue type.

(legend continued on next page)

cardiac adipose tissue located underneath the epicardial layer, vascularized by coronary vessels, and exhibiting hallmarks of metabolically active beige fat, all of which indicate evolutionary conservation between this fat depot and human eAT. Fluctuations in environmental temperature are major stressors for all organisms, endotherms, and ectotherms alike.[53,54] Some species of ectothermic vertebrates, such as fish, are, in fact, capable of warming specific tissues, most commonly the brain,[55,56] by conservation of metabolic heat from their swimming musculature[56,57] or possibly through neuronal proton gradient dissipation.[58] Our findings reveal that the heart of an ectothermic teleost could engage a different mechanism in the adaptation to cold stress via transcriptional reprogramming of the eAT to ramp up glycolysis and lipid cycling-driven thermogenesis. The ATP-consuming fatty acid-triacylglyceride cycling machinery, in which fatty acids liberated from lipolysis are constantly re-esterified to glyceride lipids, has become increasingly recognized to be the major contributor of heat production in brown adipocytes when UCP1 is lacking.[51,59–61] Upregulation of glycolytic response a to adrenergic stimulus is thought to be essential to provide glycerol backbones for the lipid cycling process.[51] Apart from serving high thermogenic demand during acute cold exposure, such an energy-expending interconversion of lipid species has been proposed to provide readily accessible pools of precursors of hormones, neurotransmitters, and signaling molecules.[62] Whether the determination of lipid availability and diversity, in addition to heat production, plays a role in maintenance of cardiac energetic homeostasis and whether the human heart utilizes the same mechanism in cold stress or other physiological challenges are key questions that require further investigation.

Several putative functions of eAT, including protection of coronary arteries from torsion, storing energy in the form of triglycerides, and buffering elevated free fatty acids in the circulation to prevent lipotoxicity in the heart, place the specialized fat depot as a critical regulator of cardiac homeostasis.[3,8,9] On the other hand, several clinical studies have strongly associated eAT with pathogenesis and progression of CAD, atrial fibrillation, and heart failure.[9] It has been proposed that loss of brown/beige adipocyte thermogenic potential in the presence of different cardiometabolic risk factors underlies such opposing roles of the fat depot.[18] Aging is a well-recognized driver of eAT morphological and functional alterations. Neonatal human eAT exhibits brown fat-like transcriptomic and phenotypic characteristics, which are remodeled during the transition to infancy.[22] Besides the change from a multilocular appearance to a more unilocular white adipocyte morphology, the most prominent changes in the transcriptional landscape of neonatal compared with infant eAT are suppression of mitochondrial components and thermogenic gene expression, with limited flexibility and responsiveness to environmental stimuli. These changes suggest a developmental program that determines induction of white adiposity and decreased mitochondrial functions in the adipose tissue.[22] In adult humans, eAT consists of seemingly uniform unilocular adipocytes even though expression of some genes related to thermogenesis persists,[6] implying a change in its primary function from dissipation to storage of energy. Although the functional transition may represent a physiological adaptation, excessive fatty acid accumulation, for example in CAD, can provoke adipocyte oxidative stress.[9,63] The cardiac fat depot of the zebrafish, in fact, gradually extends from the cardiac bulbus and atrioventricular groove in young adults (6 months) to cover the entire ventricle, similar to typical fat of adult human hearts, in aged samples (36 months).[64] Expansion of eAT is considered a sign of aging associated with cardiac fibrosis and functional insufficiency.[64] Our examination of murine eAT morphology and molecular makeup showed that aged mouse hearts, by comparison, have limited eAT coverage at the atrioventricular groove, much like young samples. Unlike human and zebrafish eAT, mouse eAT is not remarkably remodeled upon aging. The expression profile of mouse eAT, compared to that of humans and zebrafish, implies that the poorly represented eAT of animals with a fast metabolism, such as murid rodents,[65–67] may serve more intercellular paracrine signaling than metabolic functions. A mechanistic understanding of the phenotypical and transcriptomic adaptation of eAT to aging and cardiometabolic challenges is anticipated to open therapeutic opportunities for diverse cardiovascular conditions through restoration of eAT physiological and protective functions. Addition of the zebrafish model to the research toolbox would facilitate future studies in these directions.

Limitations of the study

In addition to morphological remodeling, as reported earlier, it would be important to elucidate transcriptomic reprogramming of aged zebrafish eAT to understand whether expression of different cardiac homeostatic and pathological remodeling genes is altered. This additional evidence is required, in particular, to demonstrate suitability of the teleost as a much-needed model for the studies of eAT remodeling and eAT-driven cardiac pathology. The transcriptomic profile of young zebrafish eAT suggests that the fat depot is involved in several cardiac homeostatic processes, which are not limited to metabolic functions. More work is required to functionally assess these implications and advance our understanding of the physiological role of the eAT. Additionally, expression of selected markers and thermogenic potential that differed across different pools of the epicardial adipocytes calls for elucidation of molecular signatures and functions of the distinct subpopulations. The cellular heterogeneity has not been taken into account in the bulk RNA-seq analysis provided here.

(C) Heatmap of the top 34 differentially expressed genes (DEGs) in the eAT compared with classic white fat depots, revealing a shared transcriptomic signature of the eAT across species. Shared upregulated or downregulated DEGs in zebrafish and human eATs are highlighted in black boxes.
(D) Scatterplot displaying commonly upregulated (red box) and downregulated (green box) genes in human and zebrafish eAT as well as highly expressed genes in human eAT that are downregulated in the zebrafish tissue (orange box) and vice versa (blue box).
(E) Top enriched pathway (KEGG and Reactome) of the 197 upregulated genes in zebrafish and human eAT compared with visceral (vAT) and subcutaneous (SAT) fat, respectively.
(F) KEGG pathway and Reactome analyses of the 216 downregulated genes in zebrafish vAT and human SAT compared with eAT.
Data in (D) are expressed as log2 fold change. Data in (E) and (F) are expressed as −log[P] adjusted for multiple comparisons. Data were obtained from three zebrafish eATs and vATs and four human eATs and sATs.

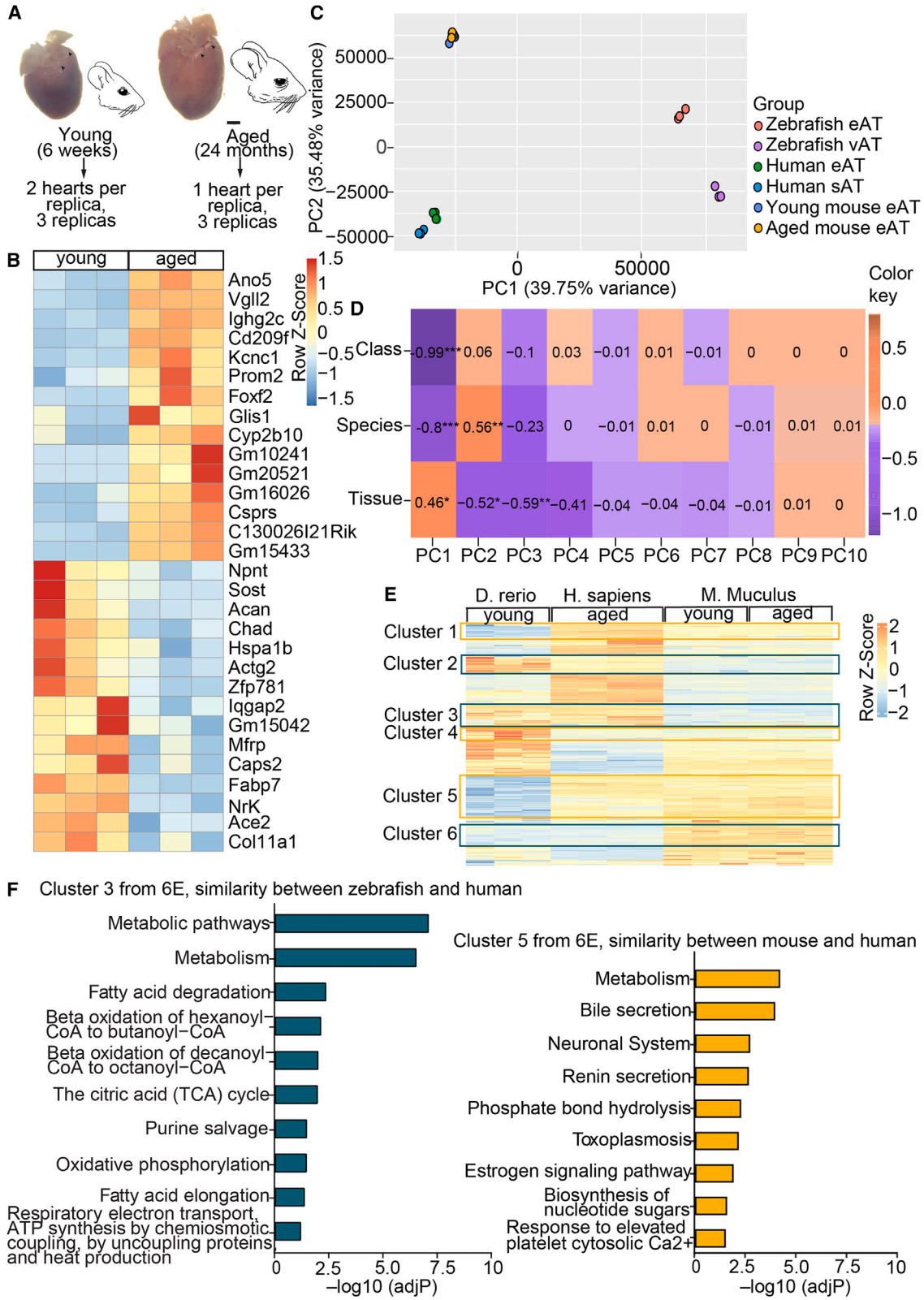

(legend on next page)

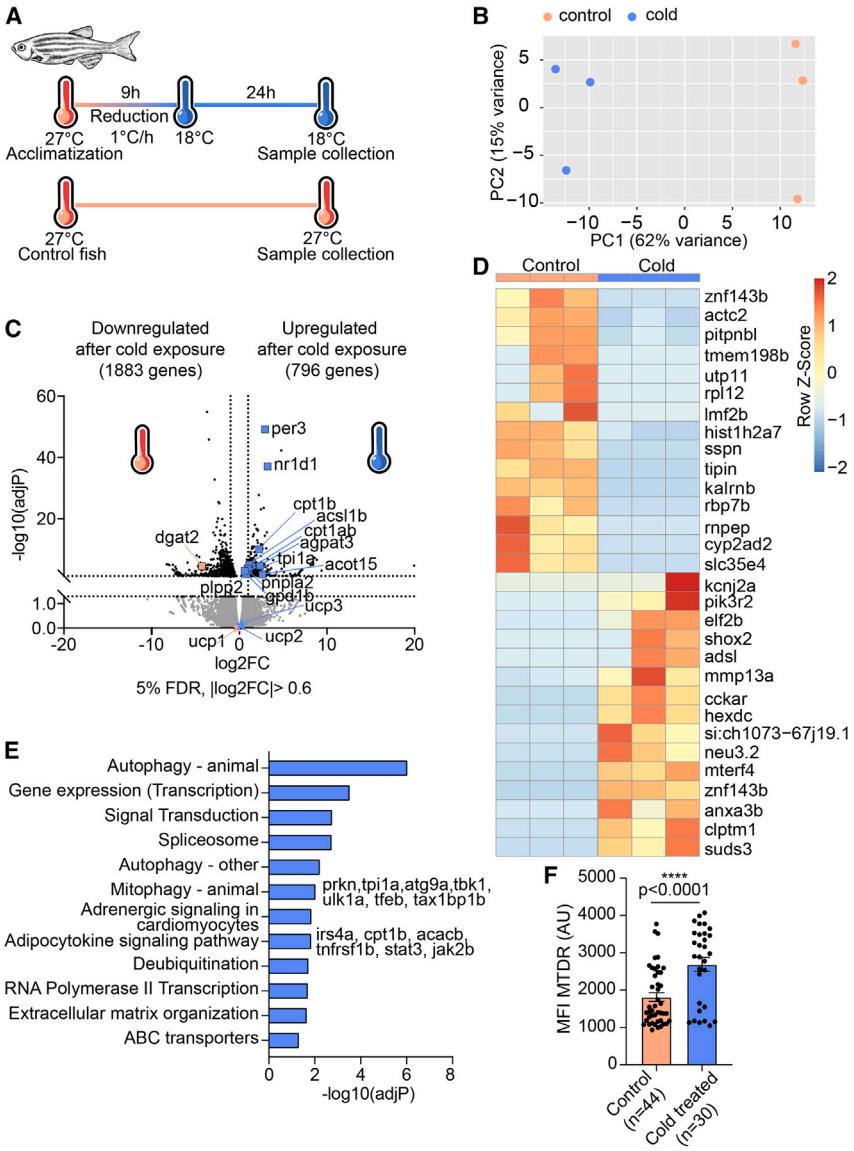

Figure 7. Cold exposure induces a lipid cycling and mitochondrial biogenesis transcriptomic program in zebrafish eAT

(A) Schematic of cold acclimatization of adult zebrafish.

(B) PCA score plot showing clustering of epicardial adipocytes according to environmental temperature.

(C) Volcano plot showing DEGs of eAT in cold-exposed compared with control siblings maintained at ambient temperature. The x axis shows log2 fold change and the y axis adjusted p value on a −log10 scale.

(D) Heatmap of the top 15 most differentially upregulated and downregulated genes in the eAT of cold-acclimatized fish.

(E) Top enriched pathways from KEGG and Reactome analyses of the upregulated genes (796) in cold-exposed fish.

(F) Bar graph depicting cold-induced elevation of active mitochondrial content in epicardial adipocytes, measured as mean fluorescent intensity of MTDR (in arbitrary units [a.u.]).

Data are presented as mean ± SEM. ****p < 0.0001, two-tailed t test. n indicates the number of adipocytes from 5 control and 3 cold-treated fish.

STAR★METHODS

Detailed methods are provided in the online version of this paper and include the following:

- KEY RESOURCES TABLE
- RESOURCE AVAILABILITY
  - Lead contact
  - Materials availability

Figure 6. Mouse epicardial adipocytes do not share the age-related metabolic remodeling trait of human eAT

(A) Schematic of RNA-seq experimental setup for young and aged mouse eAT. Arrowheads indicate the ventricular area covered by eAT. Scale bar, 1 mm.

(B) Heatmap of the top 30 DEGs in young compared with aged mouse eAT.

(C) PCA score plot showing clustering of adipocyte populations from zebrafish, mouse, and human based on the ranked expression of one-to-one orthologs.

(D) Correlation matrix of PCs with known variables. The indicated values and color gradient correspond to the Pearson correlation coefficient (r) for each pair of variables. *p < 0.05, **p < 0.01, ***p < 0.001.

(E) Clustered heatmap depicting the row-normalized ranking scores of all DEGs shared by human and zebrafish eAT compared with white adipose tissue in zebrafish, human, and mouse samples. Green boxes indicate clusters where the transcription profile is most similar between human and zebrafish and yellow boxes between human and mouse.

(F) Pathway enrichment analysis of gene clusters with similar expression in human and zebrafish (cluster 3) and similar expression in human and mouse (cluster 5). All pathway analyses were done using the KEGG and Reactome databases. Enrichment is expressed as the −log[P] adjusted for multiple comparisons.

SUPPLEMENTAL INFORMATION

Supplemental information can be found online at https://doi.org/10.1016/j.celrep.2024.113955.

ACKNOWLEDGMENTS

The authors would like to acknowledge the Flow Cytometry, Advanced Light Microscopy Technology, and Bioinformatics and Omics Data Science Technology platforms at the Max Delbrück Center for technical support and assistance. We thank the staff of the zebrafish facility for animal care. This work was supported by funding from the Helmholtz-Gemeinschaft (project VH-NG-1247) and the Deutsches Zentrum für Herz-Kreislaufforschung e.V. (DZHK) (project 81Z0100104), awarded to S.S.

AUTHOR CONTRIBUTIONS

Conceptualization, S.S.; methodology, P.-A.M.-J., I.K.-G., B.I.Z.-S., and B.P.; funding acquisition, S.S.; investigation, P.-A.M.-J., I.K.-G., B.I.Z.-S., and B.P.; project administration, A.F. and S.S.; visualization, A.F. and S.S.; supervision, A.F. and S.S.; writing – original draft, P.-A.M.-J., A.F., and S.S.; writing – review & editing, P.-A.M.-J., I.K.-G., B.I.Z.-S., B.P., A.F., and S.S.

DECLARATION OF INTERESTS

The authors declare no competing interests.

Received: April 14, 2023
Revised: January 25, 2024
Accepted: February 28, 2024
Published: March 19, 2024

REFERENCES

1. Rabkin, S.W. (2007). Epicardial fat: Properties, function and relationship to obesity. Obes. Rev. *8*, 253–261. https://doi.org/10.1111/j.1467-789X.2006.00293.x.
2. Shirani, J., Berezowski, K., and Roberts, W.C. (1995). Quantitative measurement of normal and excessive (cor adiposum) subepicardial adipose tissue, its clinical significance, and its effect on electrocardiographic QRS voltage. Am. J. Cardiol. *76*, 414–418. https://doi.org/10.1016/S0002-9149(99)80116-7.
3. Chechi, K., and Richard, D. (2015). Thermogenic potential and physiological relevance of human epicardial adipose tissue. Int. J. Obes. Suppl. *5*, S28–S34. https://doi.org/10.1038/ijosup.2015.8.
4. McAninch, E.A., Fonseca, T.L., Poggioli, R., Panos, A.L., Salerno, T.A., Deng, Y., Li, Y., Bianco, A.C., and Iacobellis, G. (2015). Epicardial adipose tissue has a unique transcriptome modified in severe coronary artery disease. Obesity *23*, 1267–1278. https://doi.org/10.1002/oby.21059.
5. Sacks, H.S., Fain, J.N., Holman, B., Cheema, P., Chary, A., Parks, F., Karas, J., Optican, R., Bahouth, S.W., Garrett, E., et al. (2009). Uncoupling protein-1 and related messenger ribonucleic acids in human epicardial and other adipose tissues: Epicardial fat functioning as brown fat. J. Clin. Endocrinol. Metab. *94*, 3611–3615. https://doi.org/10.1210/jc.2009-0571.
6. Sacks, H.S., Fain, J.N., Bahouth, S.W., Ojha, S., Frontini, A., Budge, H., Cinti, S., and Symonds, M.E. (2013). Adult Epicardial Fat Exhibits Beige Features. J. Clin. Endocrinol. Metab. *98*, 1448–1455. https://doi.org/10.1210/jc.2013-1265.
7. Gaborit, B., Venteclef, N., Ancel, P., Pelloux, V., Gariboldi, V., Leprince, P., Amour, J., Hatem, S.N., Jouve, E., Dutour, A., and Clément, K. (2015). Human epicardial adipose tissue has a specific transcriptomic signature depending on its anatomical peri-atrial, peri-ventricular, or peri-coronary location. Cardiovasc. Res. *108*, 62–73. https://doi.org/10.1093/cvr/cvv208.
8. Sacks, H.S., and Fain, J.N. (2007). Human epicardial adipose tissue: A review. Am. Heart J. *153*, 907–917. https://doi.org/10.1016/j.ahj.2007.03.019.
9. Iacobellis, G. (2022). Epicardial adipose tissue in contemporary cardiology. Nat. Rev. Cardiol. *19*, 593–606. https://doi.org/10.1038/s41569-022-00679-9.
10. Raggi, P., and Alakija, P. (2013). Epicardial adipose tissue: a long-overlooked marker of risk of cardiovascular disease. Atherosclerosis *229*, 32–33. https://doi.org/10.1016/j.atherosclerosis.2013.02.030.
11. Yamaguchi, Y., Cavallero, S., Patterson, M., Shen, H., Xu, J., Kumar, S.R., and Sucov, H.M. (2015). Adipogenesis and epicardial adipose tissue: A novel fate of the epicardium induced by mesenchymal transformation and PPARγ activation. Proc. Natl. Acad. Sci. USA *112*, 2070–2075. https://doi.org/10.1073/pnas.1417232112.
12. Rietdorf, K., and MacQueen, H. (2017). Investigating interactions between epicardial adipose tissue and cardiac myocytes: what can we learn from different approaches? Br. J. Pharmacol. *174*, 3542–3560. https://doi.org/10.1111/bph.13678.
13. Chechi, K., Vijay, J., Voisine, P., Mathieu, P., Bossé, Y., Tchernof, A., Grundberg, E., and Richard, D. (2019). UCP1 expression–associated gene signatures of human epicardial adipose tissue. JCI Insight *4*, e123618. https://doi.org/10.1172/jci.insight.123618.
14. Bartelt, A., Bruns, O.T., Reimer, R., Hohenberg, H., Ittrich, H., Peldschus, K., Kaul, M.G., Tromsdorf, U.I., Weller, H., Waurisch, C., et al. (2011). Brown adipose tissue activity controls triglyceride clearance. Nat. Med. *17*, 200–205. https://doi.org/10.1038/nm.2297.
15. Bartelt, A., John, C., Schaltenberg, N., Berbée, J.F.P., Worthmann, A., Cherradi, M.L., Schlein, C., Piepenburg, J., Boon, M.R., Rinninger, F., et al. (2017). Thermogenic adipocytes promote HDL turnover and reverse cholesterol transport. Nat. Commun. *8*, 15010. https://doi.org/10.1038/ncomms15010.
16. Klingenspor, M., Fromme, T., Hughes, D.A., Manzke, L., Polymeropoulos, E., Riemann, T., Trzcionka, M., Hirschberg, V., and Jastroch, M. (2008). An ancient look at UCP1. Biochim. Biophys. Acta *1777*, 637–641. https://doi.org/10.1016/j.bbabio.2008.03.006.
17. Jastroch, M., Buckingham, J.A., Helwig, M., Klingenspor, M., and Brand, M.D. (2007). Functional characterisation of UCP1 in the common carp: Uncoupling activity in liver mitochondria and cold-induced expression in the

brain. J. Comp. Physiol. B *177*, 743–752. https://doi.org/10.1007/s00360-007-0171-6.

18. Tseng, Y.-C., Chen, R.-D., Lucassen, M., Schmidt, M.M., Dringen, R., Abele, D., and Hwang, P.-P. (2011). Exploring Uncoupling Proteins and Antioxidant Mechanisms under Acute Cold Exposure in Brains of Fish. PLoS One *6*, e18180.
19. Xu, X., Ma, A., Li, T., Cui, W., Wang, X., Li, J., Li, Q., and Pang, Y. (2021). Genetic and Functional Characterization of Novel Brown-Like Adipocytes Around the Lamprey Brain. Front. Cell Dev. Biol. *9*, 674939–675014. https://doi.org/10.3389/fcell.2021.674939.
20. Iacobellis, G. (2021). Aging Effects on Epicardial Adipose Tissue. Front. Aging *2*, 666260. https://doi.org/10.3389/fragi.2021.666260.
21. Fei, J., Cook, C., Blough, E., and Santanam, N. (2010). Age and sex mediated changes in epicardial fat adipokines. Atherosclerosis *212*, 488–494. https://doi.org/10.1016/j.atherosclerosis.2010.06.044.
22. Ojha, S., Fainberg, H.P., Wilson, V., Pelella, G., Castellanos, M., May, S.T., Lotto, A.A., Sacks, H., Symonds, M.E., and Budge, H. (2016). Gene pathway development in human epicardial adipose tissue during early life. JCI insight *1*, e87460. https://doi.org/10.1172/jci.insight.87460.
23. Fainberg, H.P., Birtwistle, M., Alagal, R., Alhaddad, A., Pope, M., Davies, G., Woods, R., Castellanos, M., May, S.T., Ortori, C.A., et al. (2018). Transcriptional analysis of adipose tissue during development reveals depot-specific responsiveness to maternal dietary supplementation. Sci. Rep. *8*, 9628. https://doi.org/10.1038/s41598-018-27376-3.
24. Perez-Miguelsanz, J., Jiménez-Ortega, V., Cano-Barquilla, P., Garaulet, M., Esquifino, A.I., Varela-Moreiras, G., and Fernández-Mateos, P. (2021). Early Appearance of Epicardial Adipose Tissue through Human Development. Nutrients *13*, 2906. https://doi.org/10.3390/nu13092906.
25. Chau, Y.-Y., Bandiera, R., Serrels, A., Martínez-Estrada, O.M., Qing, W., Lee, M., Slight, J., Thornburn, A., Berry, R., McHaffie, S., et al. (2014). Visceral and subcutaneous fat have different origins and evidence supports a mesothelial source. Nat. Cell Biol. *16*, 367–375. https://doi.org/10.1038/ncb2922.
26. Liu, Q., Huang, X., Oh, J.-H., Lin, R.-Z., Duan, S., Yu, Y., Yang, R., Qiu, J., Melero-Martin, J.M., Pu, W.T., and Zhou, B. (2014). Epicardium-to-fat transition in injured heart. Cell Res. *24*, 1367–1369. https://doi.org/10.1038/cr.2014.125.
27. Minchin, J.E.N., and Rawls, J.F. (2017). A classification system for zebrafish adipose tissues. Dis. Model. Mech. *10*, 797–809. https://doi.org/10.1242/dmm.025759.
28. Wikstrom, J.D., Mahdaviani, K., Liesa, M., Sereda, S.B., Si, Y., Las, G., Twig, G., Petrovic, N., Zingaretti, C., Graham, A., et al. (2014). Hormone-induced mitochondrial fission is utilized by brown adipocytes as an amplification pathway for energy expenditure. EMBO J. *33*, 418–436. https://doi.org/10.1002/embj.201385014.
29. Pisani, D.F., Barquissau, V., Chambard, J.C., Beuzelin, D., Ghandour, R.A., Giroud, M., Mairal, A., Pagnotta, S., Cinti, S., Langin, D., and Amri, E.Z. (2018). Mitochondrial fission is associated with UCP1 activity in human brite/beige adipocytes. Mol. Metabol. *7*, 35–44. https://doi.org/10.1016/j.molmet.2017.11.007.
30. Meng, X.-Y., Wang, D.-D., Xie, T.-R., Yang, R.-Z., Liu, C.-F., Liu, D.-H., Li, S.-A., Luan, Y., and Kang, J.-S. (2022). A sensitive mitochondrial thermometry 2.0 and the availability of thermogenic capacity of brown adipocyte. Front. Physiol. *13*, 977431. https://doi.org/10.3389/fphys.2022.977431.
31. Kriszt, R., Arai, S., Itoh, H., Lee, M.H., Goralczyk, A.G., Ang, X.M., Cypess, A.M., White, A.P., Shamsi, F., Xue, R., et al. (2017). Optical visualisation of thermogenesis in stimulated single-cell brown adipocytes. Sci. Rep. *7*, 1383–1414. https://doi.org/10.1038/s41598-017-00291-9.
32. Nguyen, H.P., Yi, D., Lin, F., Viscarra, J.A., Tabuchi, C., Ngo, K., Shin, G., Lee, A.Y.-F., Wang, Y., and Sul, H.S. (2020). Aifm2, a NADH Oxidase, Supports Robust Glycolysis and Is Required for Cold- and Diet-Induced Thermogenesis. Mol. Cell *77*, 600–617.e4. https://doi.org/10.1016/j.molcel.2019.12.002.
33. Hou, Y., Kitaguchi, T., Kriszt, R., Tseng, Y.H., Raghunath, M., and Suzuki, M. (2017). Ca2+-associated triphasic pH changes in mitochondria during brown adipocyte activation. Mol. Metabol. *6*, 797–808. https://doi.org/10.1016/j.molmet.2017.05.013.
34. Li, J., Pan, X., Pan, G., Song, Z., He, Y., Zhang, S., Ye, X., Yang, X., Xie, E., Wang, X., et al. (2020). Transferrin Receptor 1 Regulates Thermogenic Capacity and Cell Fate in Brown/Beige Adipocytes. Adv. Sci. *7*, 1903366. https://doi.org/10.1002/advs.201903366.
35. Ikeda, K., Kang, Q., Yoneshiro, T., Camporez, J.P., Maki, H., Homma, M., Shinoda, K., Chen, Y., Lu, X., Maretich, P., et al. (2017). UCP1-independent signaling involving SERCA2bmediated calcium cycling regulates beige fat thermogenesis and systemic glucose homeostasis. Nat. Med. *23*, 1454–1465. https://doi.org/10.1038/nm.4429.
36. Jiang, D.S., Zeng, H.L., Li, R., Huo, B., Su, Y.S., Fang, J., Yang, Q., Liu, L.G., Hu, M., Cheng, C., et al. (2017). Aberrant Epicardial Adipose Tissue Extracellular Matrix Remodeling in Patients with Severe Ischemic Cardiomyopathy: Insight from Comparative Quantitative Proteomics. Sci. Rep. *7*, 43787–43812. https://doi.org/10.1038/srep43787.
37. Vyas, V., Blythe, H., Wood, E.G., Sandhar, B., Sarker, S.J., Balmforth, D., Ambekar, S.G., Yap, J., Edmondson, S.J., Di Salvo, C., et al. (2021). Obesity and diabetes are major risk factors for epicardial adipose tissue inflammation. JCI Insight *6*, e145495. https://doi.org/10.1172/jci.insight.145495.
38. Long, J.Z., Svensson, K.J., Tsai, L., Zeng, X., Roh, H.C., Kong, X., Rao, R.R., Lou, J., Lokurkar, I., Baur, W., et al. (2014). A smooth muscle-like origin for beige adipocytes. Cell Metabol. *19*, 810–820. https://doi.org/10.1016/j.cmet.2014.03.025.
39. Entwisle, S., Sanchez-Gurmaches, J., Lawrence, R., Pedersen, D., Jung, S.M., Martin-Perez, M., Guilherme, A., Czech, M., Guertin, D., and Villen, J. (2018). Cold-Induced Thermogenesis Increases Acetylation on the Brown Fat Proteome and Metabolome. Preprint at bioRxiv. https://doi.org/10.1101/445718.
40. Ji, Y., Ma, Y., Shen, J., Ni, H., Lu, Y., Zhang, Y., Ma, H., Liu, C., Zhao, Y., Ding, S., et al. (2021). TBX20 Contributes to Balancing the Differentiation of Perivascular Adipose-Derived Stem Cells to Vascular Lineages and Neointimal Hyperplasia. Front. Cell Dev. Biol. *9*, 662704. https://doi.org/10.3389/fcell.2021.662704.
41. Sáenz de Urturi, D., Buqué, X., Porteiro, B., Folgueira, C., Mora, A., Delgado, T.C., Prieto-Fernández, E., Olaizola, P., Gómez-Santos, B., Apodaka-Biguri, M., et al. (2022). Methionine adenosyltransferase 1a antisense oligonucleotides activate the liver-brown adipose tissue axis preventing obesity and associated hepatosteatosis. Nat. Commun. *13*, 1096. https://doi.org/10.1038/s41467-022-28749-z.
42. Asnicar, M.A., Köster, A., Heiman, M.L., Tinsley, F., Smith, D.P., Galbreath, E., Fox, N., Ma, Y.L., Blum, W.F., and Hsiung, H.M. (2002). Vasoactive intestinal polypeptide/pituitary adenylate cyclase-activating peptide receptor 2 deficiency in mice results in growth retardation and increased basal metabolic rate. Endocrinology *143*, 3994–4006. https://doi.org/10.1210/en.2002-220354.
43. Alessi, M.-C., Nicaud, V., Scroyen, I., Lange, C., Saut, N., Fumeron, F., Marre, M., Lantieri, O., Fontaine-Bisson, B., Juhan-Vague, I., et al. (2011). Association of vitronectin and plasminogen activator inhibitor-1 levels with the risk of metabolic syndrome and type 2 diabetes mellitus. Results from the D.E.S.I.R. prospective cohort. Thromb. Haemostasis *106*, 416–422. https://doi.org/10.1160/TH11-03-0179.
44. Hermann, P., Armant, M., Brown, E., Rubio, M., Ishihara, H., Ulrich, D., Caspary, R.G., Lindberg, F.P., Armitage, R., Maliszewski, C., et al. (1999). The vitronectin receptor and its associated CD47 molecule mediates proinflammatory cytokine synthesis in human monocytes by interaction with soluble CD23. J. Cell Biol. *144*, 767–775. https://doi.org/10.1083/jcb.144.4.767.

45. Hess, D.A., Strelau, K.M., Karki, A., Jiang, M., Azevedo-Pouly, A.C., Lee, A.-H., Deering, T.G., Hoang, C.Q., MacDonald, R.J., and Konieczny, S.F. (2016). MIST1 Links Secretion and Stress as both Target and Regulator of the Unfolded Protein Response. Mol. Cell Biol. *36*, 2931–2944. https://doi.org/10.1128/MCB.00366-16.

46. Han, J., Ding, Z., Zhuang, Q., Shen, L., Yang, F., Sah, S., and Wu, G. (2022). Analysis of different adipose depot gene expression in cachectic patients with gastric cancer. Nutr. Metab. *19*, 72. https://doi.org/10.1186/s12986-022-00708-x.

47. Yoshida, Y., Shimizu, I., Hsiao, Y.-T., Suda, M., Katsuumi, G., Seki, M., Suzuki, Y., Okuda, S., Soga, T., and Minamino, T. (2022). Differing impact of phosphoglycerate mutase 1-deficiency on brown and white adipose tissue. iScience *25*, 104268. https://doi.org/10.1016/j.isci.2022.104268.

48. Lehnig, A.C., Dewal, R.S., Baer, L.A., Kitching, K.M., Munoz, V.R., Arts, P.J., Sindeldecker, D.A., May, F.J., Lauritzen, H.P.M.M., Goodyear, L.J., and Stanford, K.I. (2019). Exercise Training Induces Depot-Specific Adaptations to White and Brown Adipose Tissue. iScience *11*, 425–439. https://doi.org/10.1016/j.isci.2018.12.033.

49. Hortells, L., Valiente-Alandi, I., Thomas, Z.M., Agnew, E.J., Schnell, D.J., York, A.J., Vagnozzi, R.J., Meyer, E.C., Molkentin, J.D., and Yutzey, K.E. (2020). A specialized population of Periostin-expressing cardiac fibroblasts contributes to postnatal cardiomyocyte maturation and innervation. Proc. Natl. Acad. Sci. USA *117*, 21469–21479. https://doi.org/10.1073/pnas.2009119117.

50. Landry, N.M., Cohen, S., and Dixon, I.M.C. (2018). Periostin in cardiovascular disease and development: a tale of two distinct roles. Basic Res. Cardiol. *113*, 1. https://doi.org/10.1007/s00395-017-0659-5.

51. Oeckl, J., Janovska, P., Adamcova, K., Bardova, K., Brunner, S., Dieckmann, S., Ecker, J., Fromme, T., Funda, J., Gantert, T., et al. (2022). Loss of UCP1 function augments recruitment of futile lipid cycling for thermogenesis in murine brown fat. Mol. Metabol. *61*, 101499. https://doi.org/10.1016/j.molmet.2022.101499.

52. Elemans, L.M.H., Cervera, I.P., Riley, S.E., Wafer, R., Fong, R., Tandon, P., and Minchin, J.E.N. (2019). Quantitative analyses of adiposity dynamics in zebrafish. Adipocyte *8*, 330–338. https://doi.org/10.1080/21623945.2019.1648175.

53. Malek, R.L., Sajadi, H., Abraham, J., Grundy, M.A., and Gerhard, G.S. (2004). The effects of temperature reduction on gene expression and oxidative stress in skeletal muscle from adult zebrafish. Comp. Biochem. Physiol. C Toxicol. Pharmacol. *138*, 363–373. https://doi.org/10.1016/j.cca.2004.08.014.

54. Castellani, J.W., and Young, A.J. (2016). Human physiological responses to cold exposure: Acute responses and acclimatization to prolonged exposure. Auton. Neurosci. *196*, 63–74. https://doi.org/10.1016/j.autneu.2016.02.009.

55. van den Burg, E.H., Peeters, R.R., Verhoye, M., Meek, J., Flik, G., and Van der Linden, A. (2005). Brain responses to ambient temperature fluctuations in fish: reduction of blood volume and initiation of a whole-body stress response. J. Neurophysiol. *93*, 2849–2855. https://doi.org/10.1152/jn.01113.2004.

56. Dickson, K.A., and Graham, J.B. (2004). Evolution and consequences of endothermy in fishes. Physiol. Biochem. Zool. *77*, 998–1018. https://doi.org/10.1086/423743.

57. Wegner, N.C., Snodgrass, O.E., Dewar, H., and Hyde, J.R. (2015). Whole-body endothermy in a mesopelagic fish, the opah, Lampris guttatus. Science 84 *348*, 786–789. https://doi.org/10.1126/science.aaa8902.

58. Laursen, W.J., Mastrotto, M., Pesta, D., Funk, O.H., Goodman, J.B., Merriman, D.K., Ingolia, N., Shulman, G.I., Bagriantsev, S.N., and Gracheva, E.O. (2015). Neuronal UCP1 expression suggests a mechanism for local thermogenesis during hibernation. Proc. Natl. Acad. Sci. USA *112*, 1607–1612. https://doi.org/10.1073/pnas.1421419112.

59. Veliova, M., Ferreira, C.M., Benador, I.Y., Jones, A.E., Mahdaviani, K., Brownstein, A.J., Desousa, B.R., Acín-Pérez, R., Petcherski, A., Assali, E.A., et al. (2020). Blocking mitochondrial pyruvate import in brown adipocytes induces energy wasting via lipid cycling. EMBO Rep. *21*, e49634. https://doi.org/10.15252/embr.201949634.

60. Wunderling, K., Zurkovic, J., Zink, F., Kuerschner, L., and Thiele, C. (2023). Triglyceride cycling enables modification of stored fatty acids. Nat. Metab. *5*, 699–709. https://doi.org/10.1038/s42255-023-00769-z.

61. Wolfrum, C., and Gerhart-Hines, Z. (2022). Fueling the fire of adipose thermogenesis. Science 84 *375*, 1229–1231. https://doi.org/10.1126/science.abl7108.

62. Sharma, A.K., and Wolfrum, C. (2023). Lipid cycling isn't all futile. Nat. Metab. *5*, 540–541. https://doi.org/10.1038/s42255-023-00779-x.

63. Naryzhnaya, N.V., Koshelskaya, O.A., Kologrivova, I.V., Suslova, T.E., Kharitonova, O.A., Andreev, S.L., Gorbunov, A.S., Kurbatov, B.K., and Boshchenko, A.A. (2022). Production of Reactive Oxygen Species by Epicardial Adipocytes Is Associated with an Increase in Postprandial Glycemia, Postprandial Insulin, and a Decrease in Serum Adiponectin in Patients with Severe Coronary Atherosclerosis. Biomedicines *10*, 2054. https://doi.org/10.3390/biomedicines10082054.

64. Murphy, L.B., Santos-Ledo, A., Dhanaseelan, T., Eley, L., Burns, D., Henderson, D.J., and Chaudhry, B. (2021). Exercise, programmed cell death and exhaustion of cardiomyocyte proliferation in aging. Dis. Model. Mech. *14*, dmm049013. https://doi.org/10.1242/dmm.049013.

65. Marchington, J.M., Mattacks, C.A., and Pond, C.M. (1989). Adipose tissue in the mammalian heart and pericardium: structure, foetal development and biochemical properties. Comp. Biochem. Physiol. B *94*, 225–232. https://doi.org/10.1016/0305-0491(89)90337-4.

66. Bale, L.K., West, S.A., and Conover, C.A. (2018). Characterization of mouse pericardial fat: regulation by PAPP-A. Growth Hormone IGF Res. *42–43*, 1–7. https://doi.org/10.1016/j.ghir.2018.07.002.

67. Iacobellis, G. (2015). Local and systemic effects of the multifaceted epicardial adipose tissue depot. Nat. Rev. Endocrinol. *11*, 363–371. https://doi.org/10.1038/nrendo.2015.58.

68. Chi, N.C., Shaw, R.M., De Val, S., Kang, G., Jan, L.Y., Black, B.L., and Stainier, D.Y.R. (2008). Foxn4 directly regulates tbx2b expression and atrioventricular canal formation. Genes Dev. *22*, 734–739. https://doi.org/10.1101/gad.1629408.

69. Kikuchi, K., Gupta, V., Wang, J., Holdway, J.E., Wills, A.A., Fang, Y., and Poss, K.D. (2011). tcf21+ epicardial cells adopt non-myocardial fates during zebrafish heart development and regeneration. Development *138*, 2895–2902. https://doi.org/10.1242/dev.067041.

70. Mosimann, C., Kaufman, C.K., Li, P., Pugach, E.K., Tamplin, O.J., and Zon, L.I. (2011). Ubiquitous transgene expression and Cre-based recombination driven by the ubiquitin promoter in zebrafish. Development *138*, 169–177. https://doi.org/10.1242/dev.059345.

71. Apaydin, D.C., Jaramillo, P.A.M., Corradi, L., Cosco, F., Rathjen, F.G., Kammertoens, T., Filosa, A., and Sawamiphak, S. (2020). Early-Life Stress Regulates Cardiac Development through an IL-4-Glucocorticoid Signaling Balance. Cell Rep. *33*, 108404. https://doi.org/10.1016/J.CELREP.2020.108404.

72. Ke, M.T., and Imai, T. (2014). Optical clearing of fixed brain samples using SeeDB. Curr. Protoc. Neurosci. *66*, 1–19. https://doi.org/10.1002/0471142301.ns0222s66.

73. Cao, J., and Poss, K.D. (2016). Explant culture of adult zebrafish hearts for epicardial regeneration studies. Nat. Protoc. *11*, 872–881. https://doi.org/10.1038/nprot.2016.049.

74. Almazloum, A., and Khalil, H. (2023). Isolation of Adult Mouse Cardiac Fibroblasts. Curr. Protoc. *3*, e840. https://doi.org/10.1002/cpz1.840.

75. Wurmus, R., Uyar, B., Osberg, B., Franke, V., Gosdschan, A., Wreczycka, K., Ronen, J., and Akalin, A. (2018). PiGx: Reproducible genomics analysis pipelines with GNU Guix. GigaScience *7*, giy123–14. https://doi.org/10.1093/gigascience/giy123.

76. Cunningham, F., Allen, J.E., Allen, J., Alvarez-Jarreta, J., Amode, M.R., Armean, I.M., Austine-Orimoloye, O., Azov, A.G., Barnes, I., Bennett, R.,

et al. (2022). Ensembl 2022. Nucleic Acids Res. *50*, D988–D995. https://doi.org/10.1093/nar/gkab1049.

77. Dobin, A., Davis, C.A., Schlesinger, F., Drenkow, J., Zaleski, C., Jha, S., Batut, P., Chaisson, M., and Gingeras, T.R. (2013). STAR: Ultrafast universal RNA-seq aligner. Bioinformatics *29*, 15–21. https://doi.org/10.1093/bioinformatics/bts635.
78. Lawrence, M., Huber, W., Pagès, H., Aboyoun, P., Carlson, M., Gentleman, R., Morgan, M.T., and Carey, V.J. (2013). Software for Computing and Annotating Genomic Ranges. PLoS Comput. Biol. *9*, 10031188–e1003210. https://doi.org/10.1371/journal.pcbi.1003118.
79. Love, M.I., Huber, W., and Anders, S. (2014). Moderated estimation of fold change and dispersion for RNA-seq data with DESeq2. Genome Biol. *15*, 550–621. https://doi.org/10.1186/s13059-014-0550-8.
80. Kolberg, L., Raudvere, U., Kuzmin, I., Vilo, J., and Peterson, H. (2020). gprofiler2 – an R package for gene list functional enrichment analysis and namespace conversion toolset g: Profiler. F1000Res. *9*, ELIXIR-709–727. https://doi.org/10.12688/f1000research.24956.2.
81. Kanehisa, M., and Goto, S. (2000). KEGG: Kyoto Encyclopedia of Genes and Genomes. Nucleic Acids Res. *28*, 27–30. https://doi.org/10.1093/nar/28.1.27.
82. Gillespie, M., Jassal, B., Stephan, R., Milacic, M., Rothfels, K., Senff-Ribeiro, A., Griss, J., Sevilla, C., Matthews, L., Gong, C., et al. (2022). The reactome pathway knowledgebase 2022. Nucleic Acids Res. *50*, D687–D692. https://doi.org/10.1093/nar/gkab1028.
83. Blighe, K., and Lun, A. (2023). PCAtools: Everything Principal Components Analysis, >,Rpackageversion2.12.0. https://doi.org/10.18129/B9.bioc.PCAtools. https://bioconductor.org/packages/PCAtools.
84. Kolde, R. (2019). Pretty Heatmaps. R Package Version 1.0.12. https://CRAN.R-project.org/pacage=pheatmap.

STAR★METHODS

KEY RESOURCES TABLE

REAGENT or RESOURCE	SOURCE	IDENTIFIER
Antibodies		
Rabbit anti-UCP1 [EPR23004-34] antibody	Abcam	Cat#ab234430; RRID:AB_2905638
Rabbit anti-Aldh1a2 antibody	GeneTex	Cat#GTX124302; RRID:AB_11177627
Mouse anti-Acetylated Tubulin [6-11B-1] antibody	Sigma-Aldrich	Cat#T6793; RRID:AB_477585
Rabbit anti-HOXC8 antibody	Thermo Fisher Scientific	Cat#PA5-41629; RRID:AB_2608983
Rabbit anti-HOXC9 antibody	Aviva Systems Biology	Cat#ARP35813_T100; RRID:AB_938161
Rabbit anti-PDRM16 antibody	Bio-Techne	Cat#NBP2-58350
Rat anti-mCherry antibody	Thermo Fisher Scientific	Cat#M11217; RRID:AB_2536611
Mouse anti-Tbx20 antibody	Sigma-Aldrich	Cat#SAB1409545
Mouse anti-Cardiac Troponin T [1F11] antibody	GeneTex	Cat#GTX10214; RRID:AB_380930
Alexa fluor anti-mouse 647	Cell Signaling Technology	Cat#4410; RRID:AB_1904023
Alexa fluor anti-rabbit 488	Cell Signaling Technology	Cat#4412; RRID:AB_1904025
Alexa fluor anti-rabbit 555	Cell Signaling Technology	Cat# 4413; RRID:AB_10694110
Alexa fluor anti-rabbit 647	Molecular Probes	Cat#A-31573; RRID:AB_2536183
Alexa fluor anti-rat 488	Molecular Probes	Cat#A-11006; RRID:AB_141373
Biological samples		
Young and aged hearts from female C57BL/6JR mice.	EPO Experimentelle Pharmakologie & Onkologie Berlin-Buch GmbH	https://www.epo-berlin.com/
Chemicals, peptides, and recombinant proteins		
4-hydroxytamoxifen (4-OHT)	Sigma-Aldrich	Cat# H7904
BODIPY 558/568 C12	Thermo Fisher Scientific	Cat# D3835
Tetramethylrhodamine, methyl ester, TMRM	Thermo Fisher Scientific	Cat# I34361
MitoTracker deep red	Thermo Fisher Scientific	Cat# M22426
HCS LipidTOX™ Green Neutral Lipid Stain	Thermo Fisher Scientific	Cat# H34475
(±)-Blebbistatin	Tocris	Cat# 1760
Forskolin	Sigma-Aldrich	Cat# F6886
CCCP	Sigma-Aldrich	Cat# C2759
Calcein AM UltraBlue	AAT Bioquest	Cat# 21908
ERthermAC	EMD Millipore	Cat# SCT057
Liberase TL Research Grade	Roche	Cat# 5401020001
TRIzol	Thermo Fisher Scientific	Cat# 15596026
Fetal Bovine Serum	GIBCO	Cat# 10270106
Penicillin-Streptomycin (10.000 U/ml)	Thermo Fisher Scientific	Cat# 15140122
MEM Non-Essential Amino Acids Solution (100X)	Thermo Fisher Scientific	Cat# 11140050
Primocin	InvivoGen	Cat# ant-pm-2
Deposited data		
RNAseq. Tissue: Human epicardial adipose tissue (eAT) and subcutaneous adipose tissue (sAT) Metabolic status:Lean CAD status: NCAD	https://insight.jci.org/articles/view/123618	GSE125856. Samples used for eAT: SRR8503303, SRR8503304, SRR8503305, SRR8503306. Samples used for vAT: SRR8503332, SRR8503333, SRR8503334, SRR8503335

(*Continued on next page*)

Continued

REAGENT or RESOURCE	SOURCE	IDENTIFIER
Epicardial adipose tissue vs. Visceral adipose tissue from zebrafish. RNAseq	This manuscript	GSE227670
Epicardial adipose tissue control temperature vs. Epicardial adipose tissue at 18°C. RNAseq	This manuscript	GSE227670
Young epicardial adipose tissue vs. aged epicardial adipose tissue from mouse. RNAseq	This manuscript	GSE227670
Experimental models: Organisms/strains		
Zebrafish: *Tg(kdrl:HRAS-mCherry)*^{s896}	Lab of Origin Stainier Lab	ZDB-ALT-081212-4
Zebrafish: *Tg(cryaa:EGFP; tcf21:Cre-ERT2)*^{pd42}	Lab of Origin Poss Lab	ZDB-ALT-110818-7
Zebrafish: *Tg(-3.5ubb:loxP-EGFP-loxP-mCherry)*^{cz170}*(ubi:Switch)*	Lab of Origin The Zon Lab	ZDB-ALT-110124-1
Software and algorithms		
Fiji/ImageJ	NIH	https://fiji.sc/
Imaris	Oxford Instruments	https://imaris.oxinst.com/
Prism	GraphPad Software	https://www.graphpad.com/scientific-software/prism/
FlowJo	BD (Becton, Disckinson & Company)	https://www.flowjo.com/solutions/flowjo

RESOURCE AVAILABILITY

Lead contact

Further information and requests for resources and reagents should be directed to and will be fulfilled by the lead contact, Dr. Suphansa Sawamiphak (suphansa.sawamiphak@mdc-berlin.de).

Materials availability

- This study did not generate new unique reagents.

Data and code availability

- Bulk RNA-seq data have been deposited at GEO and are publicly available as of the date of publication. Accession numbers are listed in the key resources table.
- This paper does not report original code.
- Any additional information required to reanalyze the data reported in this paper is available from the lead contact upon request.

EXPERIMENTAL MODEL AND STUDY PARTICIPANT DETAILS

Animal care and transgenic lines

Zebrafish husbandry and experiments were performed under standard conditions in accordance with ethical and animal welfare guidelines established by the Max Delbrück Center for Molecular Medicine and the Landesamt für Gesundheit und Soziales Berlin (LAGeSO Berlin), and LAGeSO approved the study. All experiments were performed on female zebrafish (3–12 months old). Fish were euthanized by immersion in ice water to induce hypothermia. Zebrafish were kept under standard conditions at 27 ± 1°C on a 14 h/10 h light/dark cycle. The following published transgenic lines were used in this study: *Tg(kdrl:HRAS-mCherry)*^{s896},[68] *Tg(cryaa:EGFP; tcf21:Cre-ERT2)*^{pd42}[69]; *Tg(-3.5ubb:loxP-EGFP-loxP-mCherry)*^{cz170}*(ubi:Switch)*.[70] For lineage tracing of adipocytes from epicardial tissue, 6 μM 4-hydroxy-tamoxifen (4OHT) was added to Danieau's medium (58 mM NaCl, 0.7 mM KCl,0.4 mM MgSO4, 0.6 mM Ca(NO3), 2.5 mM HEPES, pH adjusted to 7) containing *Tg(cryaa:EGFP; tcf21:Cre-ERT2; -3.5ubb:loxP-EGFP-loxP-mCherry)* embryos from 1 to 2 dpf.

METHOD DETAILS

Whole heart immunofluorescence staining

Immunofluorescence staining was performed according to an established protocol for whole zebrafish larvae with slight modifications.[71] Briefly, adult zebrafish hearts were dissected and fixed overnight with 4% PFA in PBS at 4°C. Fixed hearts were rinsed in PBS containing 0.3% (V/V) Triton X-100, and then transferred to a PBS solution supplemented with 2% (V/V) Triton X-100, 1% (w/v) bovine serum albumin, and 1% (v/v) normal goat serum for 48 h at 4°C with rotation. Primary antibody incubation was 3–4 days long at 4°C in 0.25% (V/V) Triton X-100, 1% (w/v) bovine serum albumin, and 1% (v/v) normal goat serum in PBS (PBS-T). Subsequently, hearts were rinsed in PBS-T and incubated with secondary antibodies in PBS-T for 3–4 days at 4°C with rotation. Finally, hearts were rinsed before proceeding with tissue clearing and mounting.

The primary antibodies used in this study were: anti-UCP-1 (1:200, Abcam, ab234430), anti-Aldh1a2 (1:200, GeneTex, GTX124302), anti-Acetylated Tubulin (1:150, SigmaAldrich, T6793), anti-HOXC8 (1:200, Thermo Fisher Scientific, PA5-41629), anti-HOXC9 (1:200, Aviva Systems Biology, ARP35813_T100), anti-PDRM16 (1:200, Bio-Techne, NBP2-58350), and anti-mCherry (1:300, Thermo Fisher Scientific, M11217).

The following Alexa fluor-conjugated secondary antibodies were used: anti-mouse Alexa 647 (1:200, Cell Signaling, 4410S), anti-rabbit Alexa 488 (1:200, Cell Signaling, 4412), anti-rabbit Alexa 647 (1:200, Molecular Probes, A-31573), anti-rat Alexa 488 (1:300, Molecular Probes, A-11006). Bodipy staining was performed before tissue fixation. The hearts were incubated for 20 min at room temperature with 1:1500 Bodipy (BODIPY 558/568 C12, Thermo Fisher Scientific, D3835).

Tissue clearing and confocal imaging

For optical clearing of heart tissue, a previously described SeeDB protocol[72] was used. Whole hearts were incubated in a series of solutions with progressively higher concentrations of fructose (20%, 40%, 60%, 80%, and 100% (w/v)) at room temperature for 2 h for every steps. Finally, the hearts were incubated in SeeDB (80.2% (w/w) fructose solution) overnight. Whole hearts were mounted in seeDB and examined with a Zeiss LSM880 NLO confocal microscope. Images were analyzed using Imaris software (Oxford Instruments)

Heart explantation and mitochondrial thermometry

Heart explant experiments were performed as described previously with slight modifications.[73] Briefly, hearts were extracted and the atria were removed. Next, hearts were transferred to a microcentrifuge tube to equilibrate in culture medium at 28.5°C with continuous shaking at 500 rpm for 15 min. The medium consisted of 3T3-L1 Basal Medium, 10% fetal bovine serum, 1% non-essential amino acids, 100 U/ml penicillin, 100 μg/mL streptomycin and Primocin (Explant medium). Specific mitochondrial thermometry was performed as previously described with slight modifications.[30] Explant hearts were stained with 250 nM MitoTracker deep red (Thermo Fisher, M22426), 50 nM Tetramethylrhodamine, methyl ester, TMRM (Thermo Fisher, I34361) in explant medium for 60 min at 28.5°C with continuous shaking. 10 μM (±)-Blebbistatin (Tocris, 1760) was also added to the staining medium to stop the heartbeat. Finally, explant hearts were washed twice with PBS and embedded in 1.5% low melting-point agarose in a glass bottom culture dish. A small perforation was made on top of the agarose in the direction of the heart, in order to facilitate drug penetration to the adipocytes.

Heat production measurement

Time lapse imaging experiments for heat production measurements were performed as previously described.[30] After staining with the mitochondria-specific thermometry dyes (MitoTracker and TMRM), the tissue was left to rest for 30 min at 28°C in explant medium containing 10 μM (±)-Blebbistatin before imaging. Time-lapse imaging was initiated to record baseline mitochondria activity for 8 min. Subsequently, Forskolin (final concentration: 50 μM; Sigma, F6886), CCCP (final concentration: 50 μM; Sigma, C2759) or vehicle solution was added to medium. Recording was continued over 120 min. Time-lapse images were acquired every 2 min in a CSU-W1 Confocal system equipped with a stage incubator (28°C) and CO2 (5%) supply. Fluorescence intensity of MitoTracker deep red or TMRM was monitored over time by manually selecting individual adipocytes as regions of interests. ImageJ software was used to measure fluorescence intensity. Thermal ratios were calculated as MitoTracker deep red/TMRM signal intensity, relative to the baseline (before adding the vehicle or the drug).

ERthermAC flow cytometry analysis

Dissociated epicardial and visceral fat depots were quickly washed and centrifuged at 100 g for 6 min. After adipocytes had floated to the top for 20 min, stromal vascular fraction was removed with a syringe needle. Floating adipocytes were transferred to a microcentrifuge tube with the culture medium at 28.5°C. Forskolin (final concentration 50 μM, Sigma, F6886) or vehicle was added to the solution for 2 h. Cells were then incubated with Calcein AM UltraBlue (AAT Bioquest, 21908), lipidTOX (Thermo Fisher, H34475) and 500 nM ERthermAC (EMD Millipore, SCT057) for 30 min prior to flow cytometry analysis with FACSAriaII machine (BD Biosciences). Analysis was performed using FlowJo 10.6.2 software.

Immunofluorescence and flow cytometry analysis of dissociated adipocytes

Dissociated epicardial adipocytes were fixed with 4% PFA for 45 min at room temperature, adipocytes were then washed with PBS buffer containing 3% BSA and 0.1% (V/V) Triton X-100 (PBST). Cells were blocked 10 min with 700 μL in blocking buffer (3% normal

goat serum, 2% BSA and 0.1% (V/V) Triton X-100 in PBS) under gentle agitation, followed by primary antibody incubation for 1.5 h at room temperature with continuous agitation in blocking buffer. Subsequently, adipocytes were incubated with Alexa fluor-conjugated secondary antibodies: anti-mouse Alexa 647 (1:600, Cell Signaling, 4410S), anti-rabbit Alexa 555 (1:600, Cell Signaling, 4413s), 1:250 lipidTOX (Thermo Fisher, H34475) and DAPI (1 μg/mL) for 1 h at room temperature. Finally, cells were washed prior flow cytometry analysis with FACSAriaII machine (BD Biosciences). Analysis was performed using FlowJo 10.6.2 software.

The primary antibodies used for flow cytometry analysis were anti-Tbx20 (1:150, Sigma, sab1409545), anti-cardiac troponin t (1:250, GeneTex, GTX10214) and anti-HOXC8 (1:200, Thermo Fisher Scientific, PA5-41629).

Electron microscopy

Small pieces of epicardial and visceral fat were fixed with freshly prepared 2% formaldehyde/2% glutaraldehyde in 0.1 M phosphate buffer over night at 4°C. Samples were stained with 1% OsO_4 for 2 h, dehydrated in a graded ethanol series and propylene oxide and embedded in Poly/Bed^R 812 (Polysciences, Inc., Eppelheim, Germany). Ultrathin sections were contrasted with uranyl acetate and lead citrate. Three different female fish were used for analysis. Sections were examined with a Thermo Fisher Morgagni electron microscope, digital images were taken with a Morada CCD camera and the iTEM software (EMSIS GmbH, Münster, Germany). For quantitative analyses of mitochondrial density and morphology, we averaged 15-18 sections per each fish. 3 fish per group were analyzed.

Cold acclimatization of adult zebrafish

Adult zebrafish were acclimated from 27°C (control temperature) to 18°C by gradual reduction of tank water at the rate of 1 °C/h with an external water chiller (TK 150, Teco S.r.l.). Cold-acclimated fish were maintained at 18 ± 1°C for 24 h, while control fish stayed at 27 ± 1°C. Fish were fed during acclimation and the water was continuously aerated. At the end of the 24h treatment, hearts were isolated and eAT was used for RNA sequencing or to culture as explant for live imaging.

Isolation and sequencing of RNA from zebrafish adipocytes

After centrifugation, cells from the stromal vascular fraction were separated from adipocytes as previously described with slight modifications.[36] Briefly, visceral and epicardial fat were digested using Liberase TL (Roche, 5401020001) for 30 min at 37°C, with gentle shaking. After dissociation, epicardial and visceral fat samples were quickly washed and centrifuged at 150 g for 10 min. After 30 min, floating adipocytes were collected for RNA extraction. Total RNA was prepared using TRIzol (Life Technologies, 15596026) and processed for next generation sequencing.

Isolation and sequencing of RNA from mouse epicardial adipocytes

Hearts of young (6 weeks old) and aged (24 months old) female C57BL/6JR mice were obtained from the company EPO Experimentelle Pharmakologie & Onkologie Berlin-Buch GmbH. Hearts were perfused with HBSS to remove blood, according to a previous protocol.[74] Periaortic arch adipose tissue and excess ventricle was manually removed in order to get a clean sample of the eAT from the atrio-ventricular groove. Mouse epicardial fat was digested using Liberase TL (Roche, 5401020001) for 40 min at 37°C, with gentle shaking. After dissociation, samples were quickly washed and centrifuged at 150 g for 10 min. After 40 min, adipocytes (upper layer) were taken and washed 3 times by free floating to remove any contamination from the stromal vascular fraction. Total RNA was prepared using TRIzol (Life Technologies, 15596026) and processed for next generation sequencing.

RNA sequencing

Libraries were prepared using SMARTer Stranded Total RNA-Seq Kit v3 (TaKaRa, 634487) and then sequenced using Illumina Novaseq 6000 or Illumina NovaSeq X plus. RNA-seq data were processed and analyzed using the PiGx-RNAseq pipeline (version 0.0.19).[75] The DNA (genome assembly version GRCz11), cDNA, and gene annotation (GTF) files for *Danio rerio* (zebrafish) were downloaded from the ENSEMBL database (version 104).[76] The raw reads were mapped to the genome using STAR aligner (version 2.7.3a).[77] Alignment-based expression at both gene and transcript level was quantified using GenomicAlignments R package[78] with ''mode = Union; ignore.strand = TRUE'', where reads aligning to ''exons'' were counted and grouped by ''gene_id''. Read count normalization and downstream analysis of differential gene expression was carried out using DESeq2 R package (version 1.32.0)[79] and GO term enrichment was computed using gProfiler2 R package (version 0.2.0).[80]

For mouse eAT, libraries were prepared using Illumina Stranded Total RNA (with rRNA depletion). After validation for sufficient concentration and appropriate fragment size, the library was sequenced using Illumina NextSeq 2000 P2. We performed pseudo-mapping to the mouse transcriptome (GRCm39, Ensembl) and distinctive transcript counts using Kallisto (v0.46.1).Transcript level counts were summarized into gene counts using Tximport (v1.22.0) and genes with over 10 counts were maintained. Read count normalization and downstream analysis of differential gene expression between young and aged epicardial adipocytes was carried out using DESeq2 R package (version 1.34.0).

Cross-species analysis

To identify similarities in gene expression between zebrafish and human eAT, we performed differential expression analysis on raw human RNA sequencing data published previously,[13] following the same pipeline we used to process our zebrafish sequencing data.

We then compared the list of genes differentially expressed in human eAT (compared to human sAT) with those differentially expressed in zebrafish eAT (compared to zebrafish vAT), focusing only on known 1-to-1 orthologues.[76] Finally, we performed pathway analysis on genes that were upregulated or downregulated in eAT of both species, using the gProfiler2 package for R[80]; with the KEGG[81] and Reactome[82] databases.

Additionally, we compared gene expression in mouse eAT to zebrafish and human eAT, using the aforementioned RNA-seq datasets. Counts for all genes were normalized to transcripts-per-million (TPM), to account for gene length and sequencing depth. To allow for cross-species comparisons, we filtered 1-to-1 orthologs present in all three species.[76] Then we ranked the resulting genes, within each sample, based on transcript count; assigning a higher score to higher-ranked genes. To focus on the differences in eAT-specific genes, we furthered filtered our gene list to include only genes present in the (previously obtained) list of differentially expressed genes, shared between human and fish. We used the resulting data to perform a PCA analysis to determine the distance between samples, using the PCAtools package,[83] and the eigencorplot function to correlate the resulting principal components to our known variables. Then, we produced a clustered heatmap, to depict and directly compare the expression patterns in all samples, using the Pheatmap package.[84] Finally, based on the heatmap, we manually selected specific clusters where expression was most similar between human and zebrafish or human and mouse, and performed pathway enrichment analysis in each one, as previously described.

QUANTIFICATION AND STATISTICAL ANALYSIS

Statistics

Statistical significance was determined using two-tailed Student's t tests in Graphpad Prism. Data are presented as mean ± standard error of the mean. Differences were considered statistically significant if $p < 0.05$. n indicates the number of animals used for experiments, unless stated otherwise.

Cell Reports, Volume *43*

Supplemental information

The zebrafish heart harbors a thermogenic beige fat depot analog of human epicardial adipose tissue

Paul-Andres Morocho-Jaramillo, Ilan Kotlar-Goldaper, Bhakti I. Zakarauskas-Seth, Bettina Purfürst, Alessandro Filosa, and Suphansa Sawamiphak

Supplemental Information

Supplementary Figures

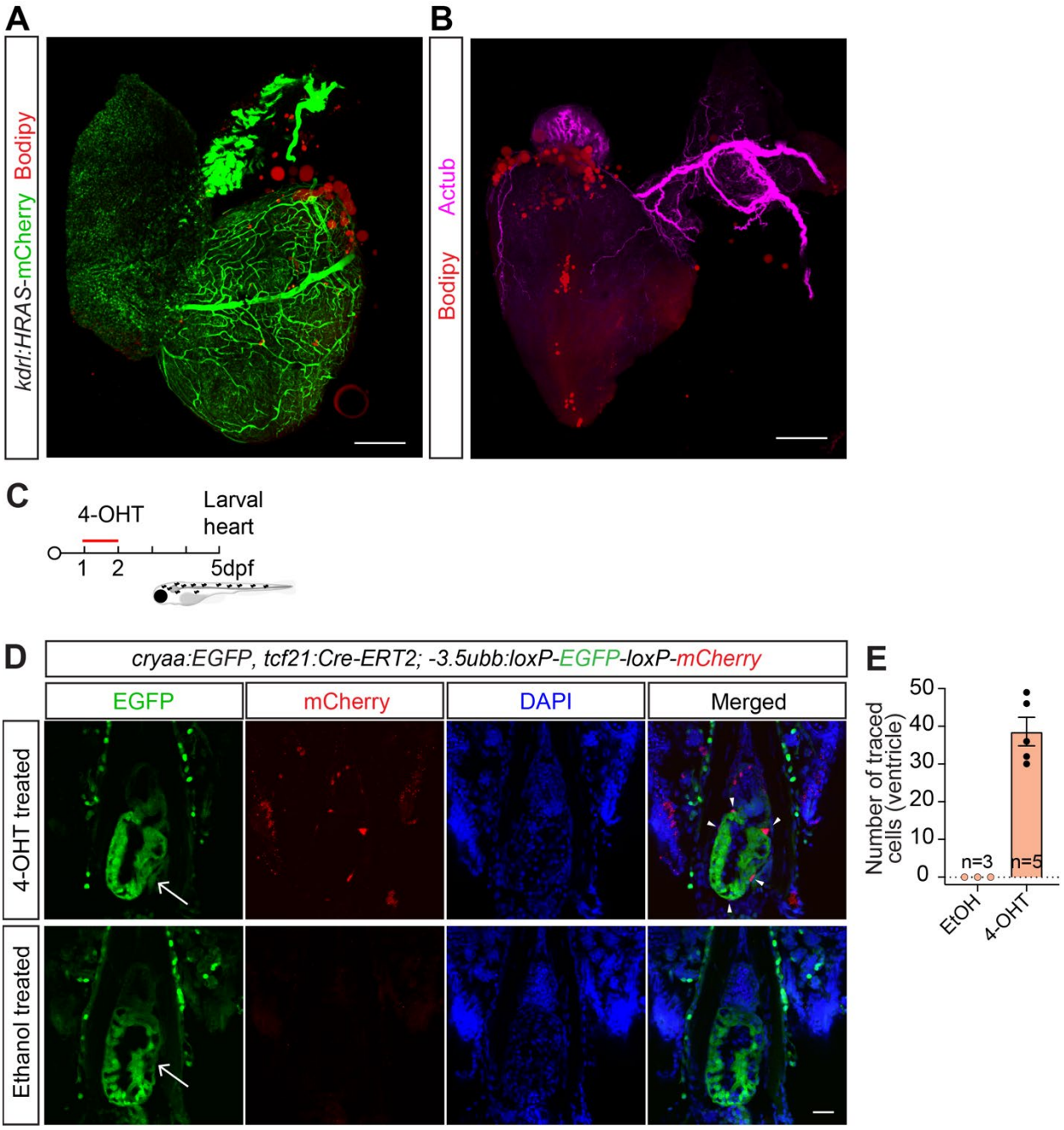

Figure S1 (related to Figure 1). Localization and lineage tracing of epicardial adipocytes in zebrafish. (A) Z-projection of a *kdrl:HRAS-mCherry* zebrafish heart,

showing vascularization of adipose tissue with coronary vessels, visualized by Bodipy staining and mCherry immunostaining, respectively. Scale bar, 200 μm. **(B)** Z-projection of a zebrafish heart, in which autonomic nerves and adipocytes were visualized by immunofluorescent staining of acetylated tubulin (Actub) and staining with Bodipy. Scale bar, 200 μm. **(C)** Schematic illustration of Cre-mediated pulse-chase lineage tracing of Tcf21+ proepicardial cells. **(D)** *cryaa:EGFP; tcf21:Cre-ERT2; ubb:loxP-EGFP-loxP-mCherry* larval hearts (arrows), treated with 4-hydroxy tamoxifen (4-OHT) and ethanol at 1-2 dpf. Ubiquitous expression of EGFP and tcf21-derived mCherry expressing cells (arrowheads) were examined by immunofluorescent staining at 5 dpf. Scale bar 30 μm. **(E)** Bar graph showing numbers of *tcf21:Cre-ERT2*-traced cells in the ventricle at 5 dpf. Data are presented as mean ± S.E.M. n indicates number of animals.

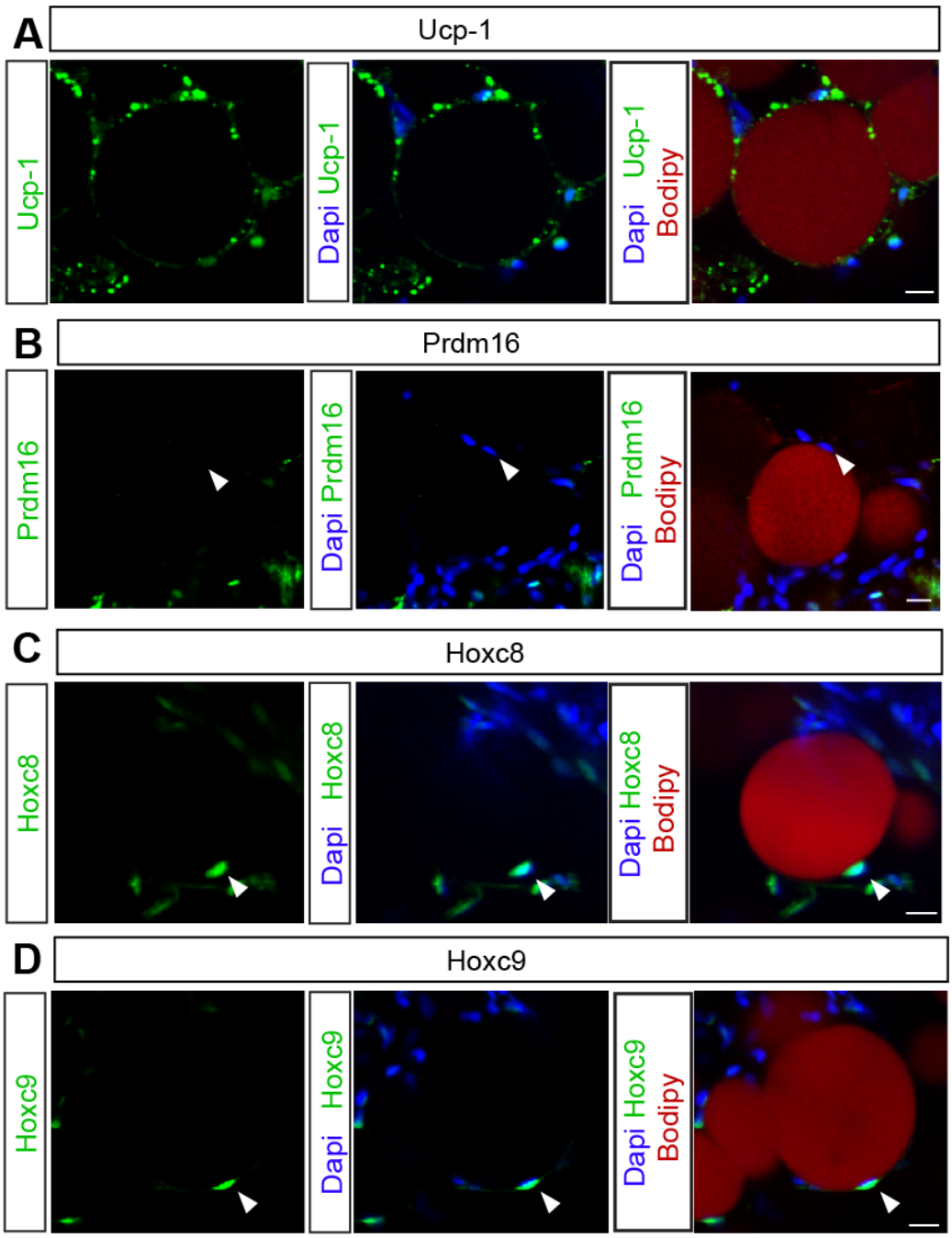

Figure S2 (related to Figure 2). Expression of white and brown adipocyte markers in zebrafish epicardial adipocytes. (A-D) Confocal images of whole-mounted zebrafish hearts, immunostained for Ucp1, Prdm16, Hoxc8, and Hoxc9, and stained with BODIPY 558/568 C12 and DAPI. White arrowheads indicate nuclear localization of the proteins in adipocytes. Scale bar, 10 μm.

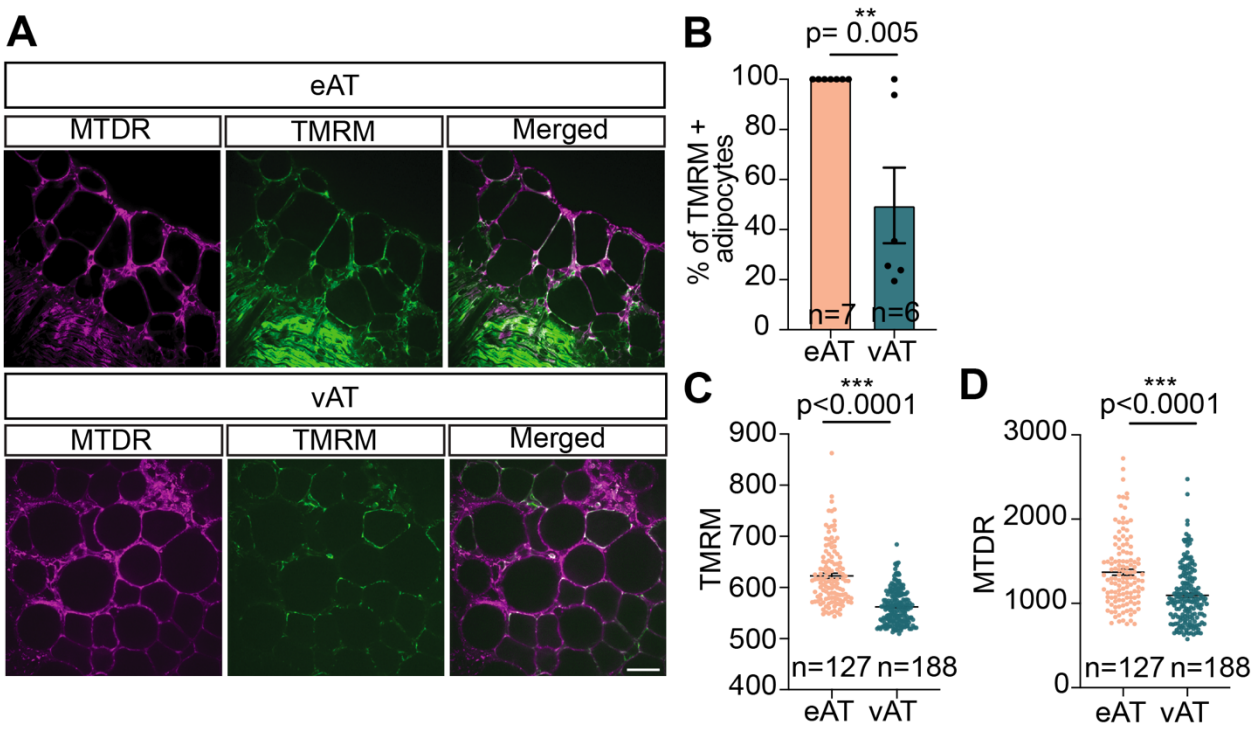

Figure S3 (related to Figure 2). **Higher content of active mitochondria in zebrafish eAT, as compared to white adipose tissue. (A)** Confocal images showing epicardial adipose tissue (eAT) and abdominal visceral adipose tissue (vAT) explants, in which active mitochondria were labelled with mitotracker deep red (MTDR) and Tetramethylrhodamine, methyl ester (TMRM). Scale bar, 50 µm. **(B)** Bar graph depicting lower percentages of TMRM-positive adipocytes in vAT explants. **(C, D)** Bar graphs depicting lower densities of TMRM **(C)** and MTDR **(D)** positive mitochondria in eAT and vAT adipocytes. n indicates number of animals in (B) or number of analyzed adypocites from five fish per condition in **(C, D)**. Data are presented as mean ± S.E.M. **p < 0.01, ***p < 0.001, two-tailed t-test. n indicates number of animals.

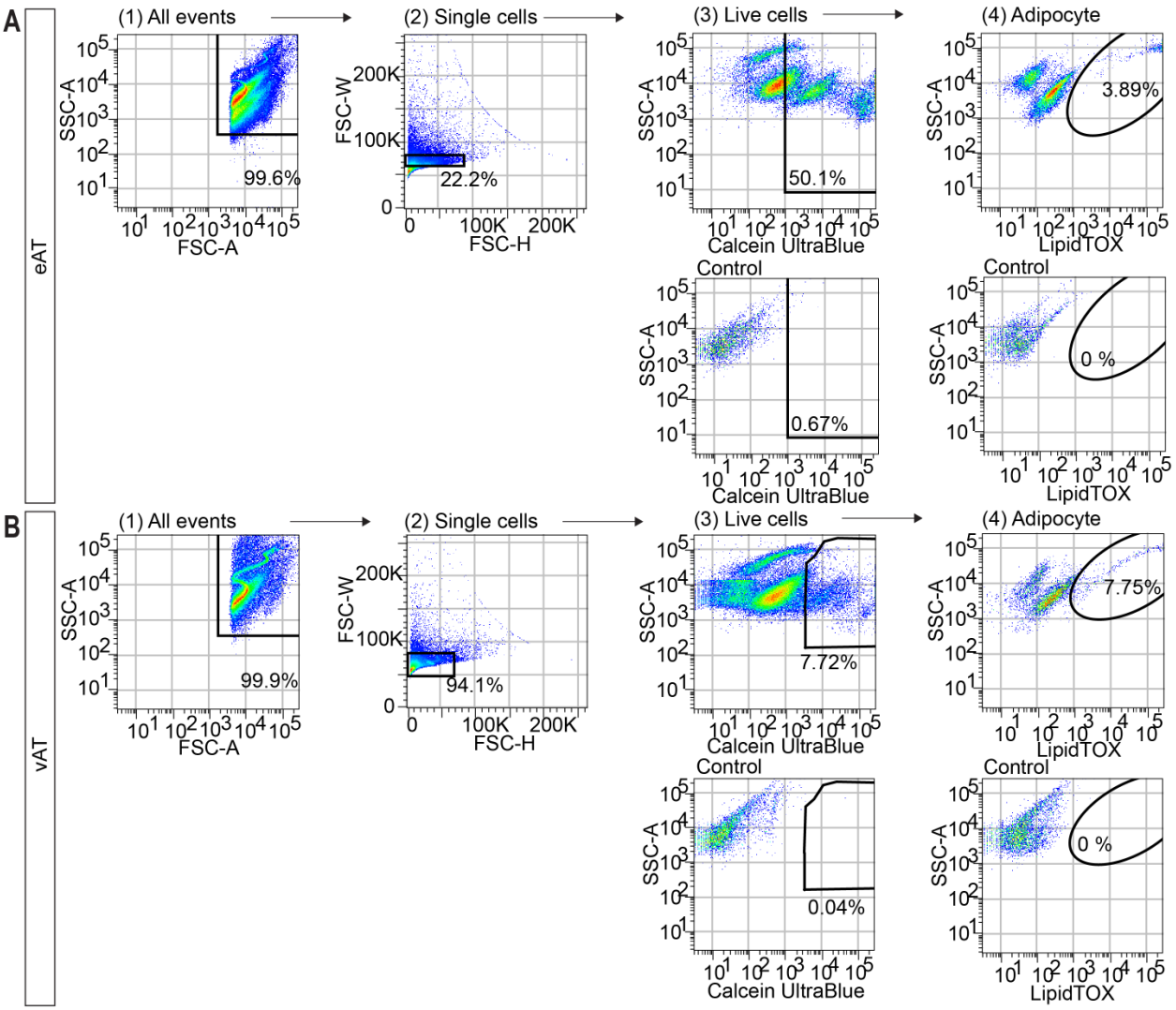

Figure S4 (related to Figure 3). **Gating strategy of adipocytes.** eAT **(A)** and vAT **(B)** were isolated by flow cytometry for analysis of thermogenesis activity by ErthermAC.

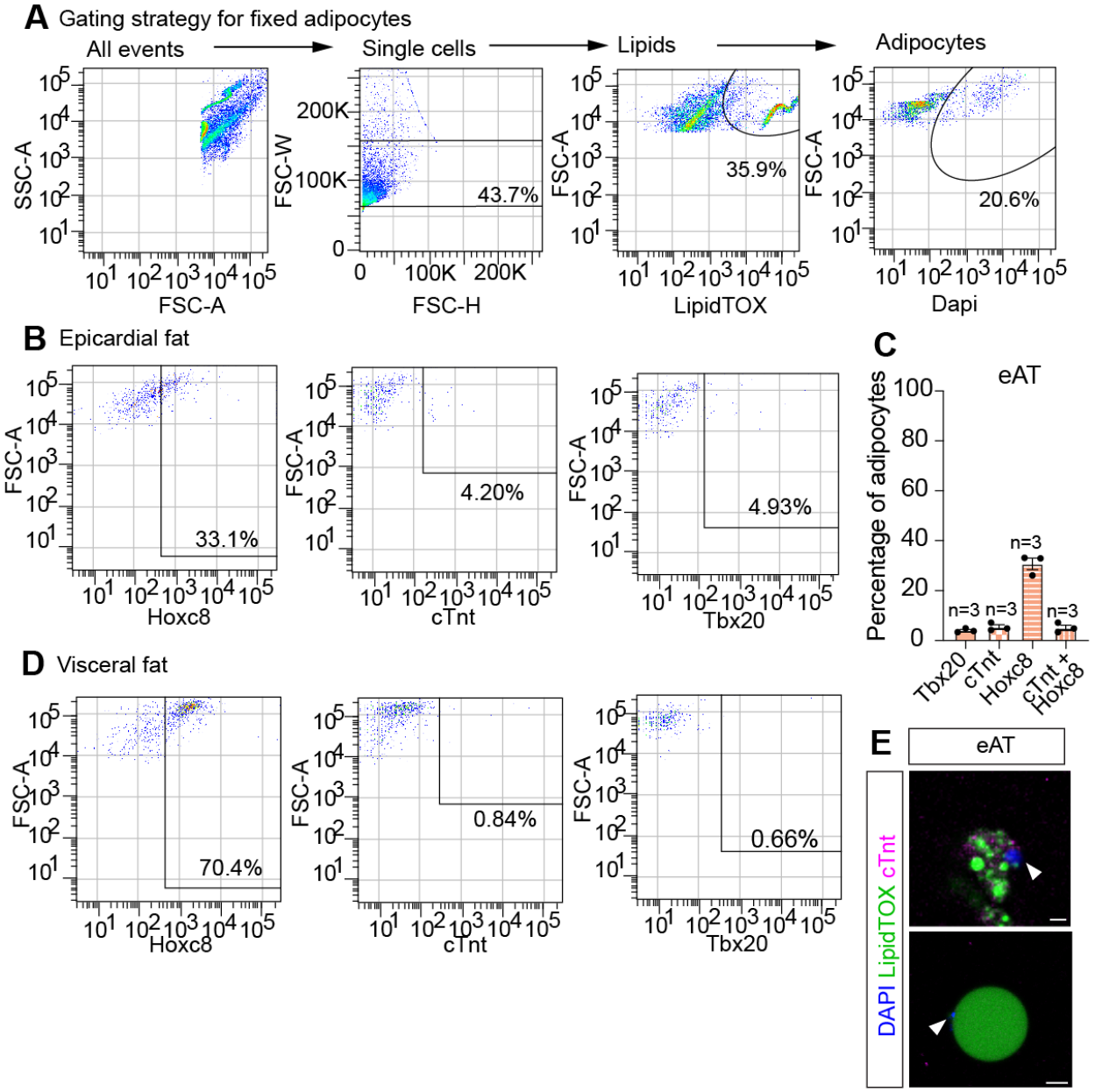

Figure S5 (related to Figure 4). Assessment of cardiac development and homeostasis gene expression in epicardial adipocytes by flow cytometry and immunofluorescence. (A and **B)** Subpopulations of adipocytes from epicardial fat, labelled with LipidTox and DAPI **(A)** express Hoxc8, cTnt, and Tbx20 **(B)**. **(C)** Bar graph depicting percentages of Hoxc8+, cTnt+, Tbx20+, and cTnt+Hoxc8+ per total adipocytes in the eAT. Data are presented as mean ± S.E.M. n indicates number of animals. **(D)**

Majority of vAT adipocytes were Hoxc8+, but did show detectable cTnt or Tbx20 expression. **(E)** Representative images of dissociated epicardial adipocytes, visualized by lipidTox accumulation, some of which express cTnt, detected by immunofluorescent staining. Arrowheads indicate adipocyte nuclei. Scale bar, 4 μm. Upper panel showed epicardial adipocyte co-expressed cTnt. cTnt was not detectable in adipocyte shown in the lower panel. White arrowheads indicates adipocyte nuclei labelled with DAPI.

Genes shown in Figure 5D

upregulated in human and zebrafish eAT (top20)

human_ID	zebrafish_ID	human_log2FC	zebrafish_log2FC
ENSG00000164532	ENSDARG00000005150	10,2211	9,3887
ENSG00000130700	ENSDARG00000017821	7,8020	1,9722
ENSG00000183421	ENSDARG00000043211	5,1737	0,4910
ENSG00000188176	ENSDARG00000055632	4,5488	4,2133
ENSG00000147573	ENSDARG00000058158	4,0264	8,7259
ENSG00000101311	ENSDARG00000052652	3,9087	0,2258
ENSG00000118526	ENSDARG00000036869	3,8240	2,4209
ENSG00000096696	ENSDARG00000076673	3,4611	1,7242
ENSG00000153820	ENSDARG00000017429	3,4018	4,8271
ENSG00000117707	ENSDARG00000055158	3,3991	1,6897
ENSG00000124772	ENSDARG00000070919	3,3840	4,3632
ENSG00000215218	ENSDARG00000079276	3,2513	7,1007
ENSG00000079931	ENSDARG00000031136	2,9777	3,5533
ENSG00000105509	ENSDARG00000042983	2,9573	5,1667
ENSG00000169071	ENSDARG00000076227	2,8838	3,2004
ENSG00000167971	ENSDARG00000046107	2,7586	0,9878
ENSG00000103888	ENSDARG00000039881	2,6991	1,8262
ENSG00000106278	ENSDARG00000020871	2,5553	4,1617
ENSG00000141639	ENSDARG00000110581	2,5456	1,6705
ENSG00000162631	ENSDARG00000073713	2,4122	0,2522

upregulated in human sAT and zebrafish vAT(top20)

human_ID	zebrafish_ID	human_log2FC	zebrafish_log2FC
ENSG00000037965	ENSDARG00000070346	-8,9036	-9,1642
ENSG00000180806	ENSDARG00000092809	-7,3938	-7,6380
ENSG00000120068	ENSDARG00000056027	-6,4626	-3,2247
ENSG00000170689	ENSDARG00000056023	-5,1066	-2,7830
ENSG00000106004	ENSDARG00000102501	-4,6856	-4,3149
ENSG00000131771	ENSDARG00000076280	-4,3914	-0,9056
ENSG00000145824	ENSDARG00000056627	-3,6315	-3,9584
ENSG00000155966	ENSDARG00000052242	-2,9630	-1,5614
ENSG00000175161	ENSDARG00000062633	-2,8711	-6,6697
ENSG00000185818	ENSDARG00000077256	-2,4250	-3,0299
ENSG00000141449	ENSDARG00000039196	-2,2469	-4,0214
ENSG00000130876	ENSDARG00000008100	-2,1133	-2,3330
ENSG00000170786	ENSDARG00000016233	-2,0903	-1,8126
ENSG00000079689	ENSDARG00000058732	-1,9503	-1,1526
ENSG00000162444	ENSDARG00000070486	-1,9401	-1,7417
ENSG00000124003	ENSDARG00000086481	-1,8104	-1,9932
ENSG00000158516	ENSDARG00000043722	-1,7426	-17,3074
ENSG00000105088	ENSDARG00000102825	-1,6073	-0,8890
ENSG00000278535	ENSDARG00000004141	-1,4856	-3,7050
ENSG00000010319	ENSDARG00000007560	-1,4552	-2,0455

upregulated in human eAT but downregulated in zebrafish eAT (top20)

human_ID	zebrafish_ID	human_log2FC	zebrafish_log2FC
ENSG00000081052	ENSDARG00000002831	4,0948	-0,8197
ENSG00000151224	ENSDARG00000039605	4,0894	-9,0946
ENSG00000078725	ENSDARG00000078302	3,7369	-0,1313
ENSG00000112486	ENSDARG00000038968	3,7304	-4,6057
ENSG00000015413	ENSDARG00000068181	3,7074	-1,3552
ENSG00000166922	ENSDARG00000032126	3,5769	-1,7886
ENSG00000109072	ENSDARG00000053831	3,4093	-4,0363
ENSG00000156510	ENSDARG00000038703	3,3469	-2,3410
ENSG00000276418	ENSDARG00000061713	3,3404	-2,5828
ENSG00000099958	ENSDARG00000033871	3,1524	-2,4378
ENSG00000106018	ENSDARG00000012353	2,9349	-6,6642
ENSG00000154639	ENSDARG00000043658	2,8708	-1,4678
ENSG00000172367	ENSDARG00000040568	2,6993	-4,1138
ENSG00000162366	ENSDARG00000017127	2,6565	-0,9768
ENSG00000160183	ENSDARG00000036545	2,6512	-4,3100
ENSG00000129354	ENSDARG00000096454	2,5621	-4,3596
ENSG00000099960	ENSDARG00000068286	2,5420	-4,3945
ENSG00000164142	ENSDARG00000061021	2,4855	-0,2819
ENSG00000005513	ENSDARG00000037782	2,4663	-5,5458
ENSG00000178882	ENSDARG00000023484	2,4145	-1,5737

upregulated in zebrafish eAT but downregulated in human eAT (top20)

human_ID	zebrafish_ID	human_log2FC	zebrafish_log2FC
ENSG00000170549	ENSDARG00000101831	-5,7771	6,1882
ENSG00000170561	ENSDARG00000001785	-4,2691	2,2609
ENSG00000143320	ENSDARG00000030449	-3,2008	2,5615
ENSG00000075035	ENSDARG00000061819	-2,8542	3,3995
ENSG00000004939	ENSDARG00000012881	-2,8294	4,6586
ENSG00000164708	ENSDARG00000057571	-2,7617	10,9069
ENSG00000150893	ENSDARG00000102626	-2,7473	3,6225
ENSG00000176842	ENSDARG00000034043	-2,4764	2,8443
ENSG00000134317	ENSDARG00000061391	-1,9848	2,1631
ENSG00000085741	ENSDARG00000014796	-1,9316	6,6748
ENSG00000133110	ENSDARG00000043806	-1,8503	8,2995
ENSG00000169047	ENSDARG00000054087	-1,7975	1,8073
ENSG00000166165	ENSDARG00000043257	-1,5554	2,1312
ENSG00000153162	ENSDARG00000015686	-1,4321	2,8131
ENSG00000158458	ENSDARG00000077818	-1,3634	1,7280
ENSG00000089225	ENSDARG00000024894	-1,2430	8,6155
ENSG00000035664	ENSDARG00000061096	-1,2353	3,6422
ENSG00000172572	ENSDARG00000004227	-1,2172	2,9232
ENSG00000166148	ENSDARG00000045788	-1,1960	2,4579
ENSG00000285854	ENSDARG00000019644	-1,1676	4,3786

Figure S6 (related to Figure 5). Top 20 most differentially expressed genes in young zebrafish and aged human eAT, as compared to classical white adipose tissues, identified by RNA sequencing (RNA-Seq). Fold changes of all orthologues, indicated by Ensembl gene IDs, are displayed as log base 2 values.

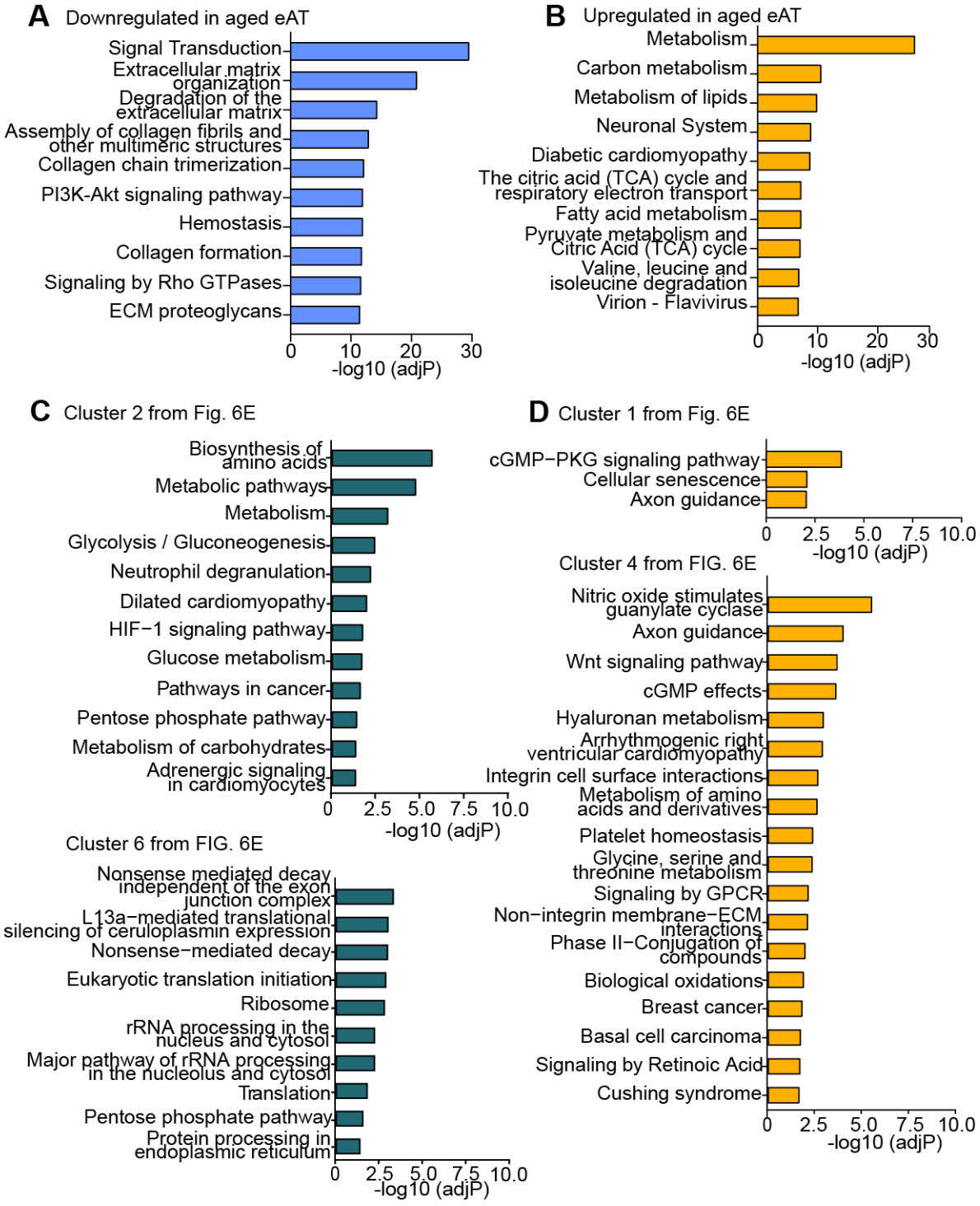

Figure S7 (related to Figure 6). Highly represented pathways of up- and downregulated genes from cross-species analysis of whole transcriptomic profile

of eAT. (A and **B)** Enriched pathways associated with downregulated **(A)** and upregulated **(B)** genes in aged as compared to young mouse eAT. **(C** and **D)** Significantly overrepresented pathways based on gene clusters with similar expression in human and zebrafish (cluster 2 and 6 from Fig. 6E) **(C)** or those with similar expression in human and mouse (cluster 1 and 4 from Fig. 6E) **(D)**. All pathway enrichment analyses were done using KEGG and REACTOME databases. Enrichment is expressed as the -log[P] adjusted for multiple comparisons. Only DEGs with log2 fold change score more than 0.6 were included in the analysis.